AGU PUBLICATIONS

Geochemistry, Geophysics, Geosystems

RESEARCH ARTICLE
10.1002/2016GC006433

Key Points:
- We present a gridded compilation of seafloor reflectivity of the Rainbow area of the Mid-Atlantic Ridge
- Variations in seafloor volcanic and tectonic features correlate with inferred magma supply
- We use correlations in backscatter amplitude and observed lithology to generate a map of Rainbow massif

Supporting Information:
- Supporting Information S1

Correspondence to:
D. Eason,
deborahe@hawaii.edu

Citation:
Eason, D. E., R. A. Dunn, J. P. Canales, and R. A. Sohn (2016), Segment-scale variations in seafloor volcanic and tectonic processes from multibeam sonar imaging, Mid-Atlantic Ridge Rainbow region (35°45′–36°35′N), *Geochem. Geophys. Geosyst.*, *17*, 3560–3579, doi:10.1002/2016GC006433.

Received 9 MAY 2016
Accepted 2 AUG 2016
Accepted article online 9 AUG 2016
Published online 7 SEP 2016

© 2016. American Geophysical Union. All Rights Reserved.

Segment-scale variations in seafloor volcanic and tectonic processes from multibeam sonar imaging, Mid-Atlantic Ridge Rainbow region (35°45′–36°35′N)

Deborah E. Eason[1], Robert A. Dunn[1], J. Pablo Canales[2], and Robert A. Sohn[2]

[1]Department of Geology and Geophysics, University of Hawaii, Honolulu, Hawaii, USA, [2]Department of Geology and Geophysics, Woods Hole Oceanographic Institution, Woods Hole, Massachusetts, USA

Abstract Along-axis variations in melt supply and thermal structure can lead to significant variations in the mode of crustal accretion at mid-ocean ridges. We examine variations in seafloor volcanic and tectonic processes on the scale of individual ridge segments in a region of the slow spreading Mid-Atlantic Ridge (35°45′–36°35′N) centered on the Rainbow nontransform discontinuity (NTD). We use multibeam sonar backscatter amplitude data, taking advantage of multifold and multidirectional coverage from the MARINER geophysical study to create a gridded compilation of seafloor reflectivity, and interpret the sonar image within the context of other data to examine seafloor properties and identify volcanic flow fields and tectonic features. Along the spreading segments, differences in volcanic productivity, faulting, eruption style, and frequency correlate with inferred magma supply. Regions of low magma supply are associated with more widely spaced faults, and larger volcanic flow fields that are more easily identified in the backscatter image. Identified flow fields with the highest backscatter occur near the ends of ridge segments. Their relatively smooth topography contrasts with the more hummocky, cone-dominated terrain that dominates most of the neovolcanic zone. Patches of seafloor with high, moderately high, and low backscatter intensity across the Rainbow massif are spatially correlated with observations of basalt, gabbro and serpentinized peridotite, and sediment, respectively. Large detachment faults have repeatedly formed along the inside corners of the Rainbow NTD, producing a series of oceanic core complexes along the wake of the NTD. A new detachment fault is currently forming in the ridge segment just north of the now inactive Rainbow massif.

1. Introduction

Variations in the relative roles of magmatic and tectonic processes at mid-ocean ridges lead to diversity in the style of crustal formation and geological character of the seafloor. Slow spreading mid-ocean ridges (MOR) such as the Mid-Atlantic Ridge tend to have lower time-averaged magma supply than faster spreading ridges, form volcanic terrains heavily modified by faulting, and display a greater degree of along-axis segmentation [e.g., *Macdonald et al.*, 1991]. Volcanic activity primarily occurs within deep, broad, rift valleys formed by large-offset normal faults and is not spatially uniform, sometimes constructing axial volcanic ridges (AVRs) within the rift valley [e.g., *Searle et al.*, 2010; *Yeo et al.*, 2012]. Because low mantle upwelling rates produce low fluxes of magma and heat to the ridge, the rate of magmatic intrusion is insufficient to alleviate tensile stresses due to plate opening, and spreading is accommodated by larger degrees of tectonic extension. Lower melt supply is generally associated with larger throw faults that are more widely spaced, and areas with long periods of low melt supply may develop detachment faults to accommodate the strain [e.g., *Tucholke et al.*, 2008]. Long-lived detachment faults may exhume lower crustal and mantle material [e.g., *Cann et al.*, 1997; *Sauter et al.*, 2013], producing dome-shaped seafloor structures known as oceanic core complexes (OCCs).

Along-axis variations in melt supply and thermal structure can lead to significant variations in crustal accretion style even within a single ridge segment [e.g., *Shaw and Lin*, 1993]. Crustal thickness tends to be highest at segment centers and decreases toward segment ends [*Tolstoy et al.*, 1993; *Hooft et al.*, 2000; *Canales et al.*, 2000; *Seher et al.*, 2010], reflecting lower magma supply at ridge offsets. This relationship is supported by petrologic studies showing evidence for higher average pressures of crystallization near segment ends, suggesting deeper magma storage and cooler lithospheric conditions near ridge offsets than at segment centers [e.g., *Grove et al.*, 1992; *Herzberg*, 2004; *Eason and Sinton*, 2006]. The decrease in magma supply

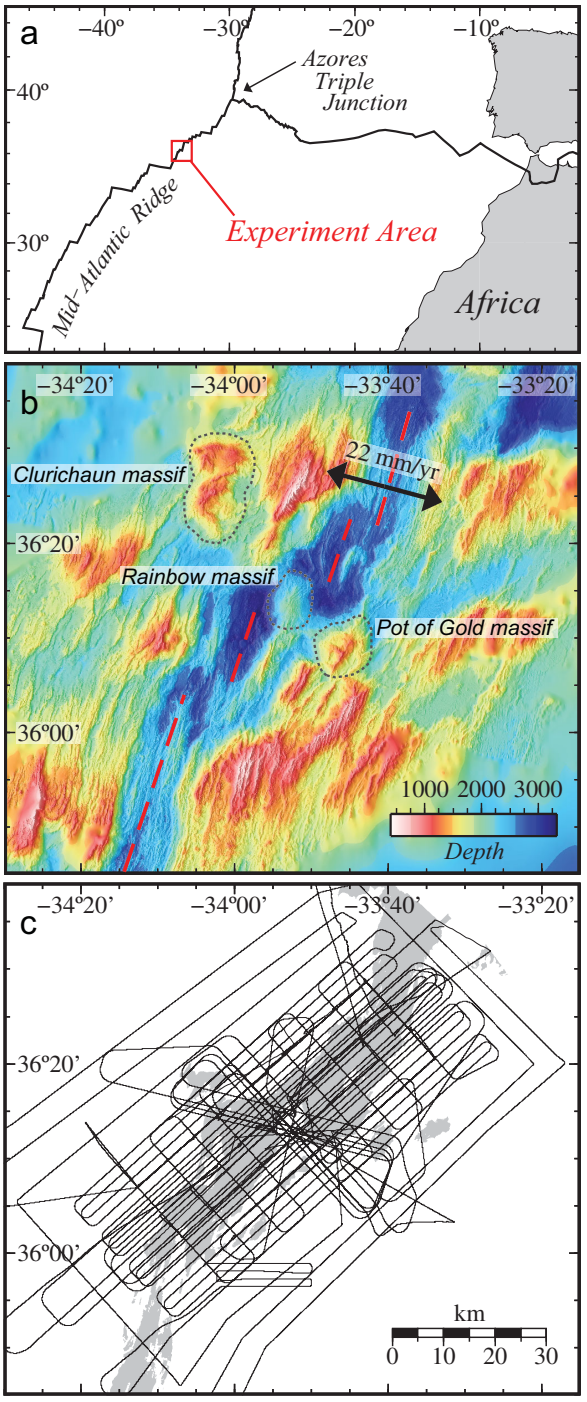

Figure 1. Maps showing (a) the experiment location, (b) a composite of satellite-derived and shipboard bathymetry [*Paulatto et al.*, 2015], and (c) ship track. (a) The study area is located 500 km south of the Azores Triple Junction on the Mid-Atlantic Ridge (36°15′N). (b) The bathymetry shows the ridge-NTD-ridge staircase geometry of the plate boundary, with dashed red lines showing the approximate locations of the ridge axes. Arrows indicate the estimated spreading direction. The locations of three principal oceanic core complexes discussed in the text are outlined by dotted lines. Dark blue colors highlight deeper portions of the ridge valley, which are located near the segment ends. (c) Black lines indicate the track of the R/V *Langseth* during the MARINER experiment (cruise MGL1305), along which the sonar data were collected. The grey shaded area represents water depths greater than 2500 m, illustrating the location of the axial valleys along the ridge segments.

toward segment ends is often accompanied by changes in faulting style as more spreading is accommodated by tectonic extension [e.g., *Shaw*, 1992; *Cannat et al.*, 1995; *Behn et al.*, 2002; *Behn and Ito*, 2008], and OCCs are more prevalent. Because they expose lower crustal and upper mantle sequences at the surface, OCCs provide important windows into magmatic and crustal accretion processes. While they have been of great interest to multiple scientific communities since their discovery [e.g., *Cann et al.*, 1997; *Tucholke et al.*, 1998; *Ildefonse et al.*, 2007; *Escartín et al.*, 2008; *Cheadle and Grimes*, 2010; *Escartín and Canales*, 2011], the factors contributing to their formation and evolution are still poorly understood.

To investigate slow spreading ridge processes, including the magmatic and tectonic conditions that lead to OCC formation and the development of vigorous hydrothermal fields, a series of marine geophysical experiments were carried out in the Rainbow area (35°45′–36°35′N) of the Mid-Atlantic Ridge including seismic surveys, gravity, magnetics, and sonar mapping [*Canales et al.*, 2013; *Paulatto et al.*, 2015]. Known collectively as the MARINER (Mid-Atlantic Ridge INtegrated Experiments at Rainbow) survey, they spanned the Rainbow OCC, including the extensive Rainbow hydrothermal field (RHF) hosted there, and the adjacent ridge segments to the north and south. The bathymetry, gravity, and magnetics data from this cruise were previously published by *Paulatto et al.* [2015], who analyzed the morphotectonic structure of the area. In this study we use the multibeam sonar backscatter amplitude data from the experiment and take advantage of its multifold and multidirectional coverage to create a gridded compilation of seafloor reflectivity. We use the resulting sonar image to examine seafloor characteristics and ridge morphology, identify ridge neovolcanic zones, including individual volcanic flow fields, and aid in interpretations of the magmatic and tectonic evolution of the spreading system.

2. Study Area

South of the Azores triple junction, the Mid-Atlantic Ridge (MAR) is divided into a series of right-stepping ridge segments between

10 and 100 km long [*Detrick et al*., 1995; *Gràcia et al*., 2000], separated by second-order nontransform discontinuities (NTDs) of the ridge axis with offsets of ~10 to ~55 km (Figure 1a). Between the Azores and the Oceanographer transform fault (~35°05′N), this pattern persists uninterrupted for roughly 600 km of the plate boundary. As such, a ridge-NTD-ridge triplet constitutes a fundamental unit of the present plate boundary, one whose character is suggested to vary due to underlying factors such as melt supply and rheology [e.g., *Detrick et al*., 1995; *Behn and Ito*, 1998; *Gràcia et al*., 2000]. From the Azores to Oceanographer, the full spreading rate varies little, from ~22 to 20 mm/yr [*DeMets et al*., 2010], and spreading is oblique to the average trend of the plate boundary, presumably controlling the "staircase" geometry of the ridge axis found here. The plate boundary exhibits low-amplitude, broad trends in gravity, bathymetry, and geochemical data [*Schilling et al*., 1983; *Detrick et al*., 1995; *Cannat et al*., 1999] associated with elevated magmatic input due to the proximity of the Azores hot spot in the north [e.g., *Detrick et al*., 1995; *Parson et al*., 2000], with decreasing hot spot influence to the south. The geochemical evidence for hot spot influence extends at least as far south as the Hayes Fracture Zone (33°40′N) [e.g., *Schilling et al*., 1983]. Superimposed on the long-wavelength trend are shorter wavelength changes that correlate with ridge-NTD-ridge segmentation, with shallower bathymetry and lower gravity located near segment centers, presumably due to higher melt supply at segment centers and lower supply at segment ends [*Phipps Morgan and Forsyth*, 1988]. The strength of these changes varies roughly proportionally to the length of the segments [*Detrick et al*., 1995].

The NTDs are generally characterized by greater seafloor depths and, unlike first-order (transform) offsets, lack a stable well-defined strike-slip fault zone [e.g., *Macdonald et al*., 1991], instead accommodating spreading between neighboring ridge segments by broad zones of strike-slip and oblique extensional faulting [*Grindlay et al*., 1991]. Many of the NTDs south of Azores are characterized by irregularly faulted massifs with ultramafic exposures [*Gràcia et al*., 2000]. The offsets are often flanked by discordant zones (or "wakes") in seafloor morphology in the older off-axis crust, suggesting they can persist for several Myr. The traces of the discordant zones indicate that the offsets migrate along the plate boundary in response to changes in the stress field and magma supply. Third and fourth-order discontinuities in the ridge axis also exist, but are smaller en-echelon offsets with little-to-no off-axis trace [*Grindlay et al*., 1991; *Sempéré et al*., 1993].

Located along the MAR between 35°45′N and 36°40′N (Figure 1b), the study area encompasses the AMAR and South AMAR (S AMAR) ridge segments, each of which includes a "minor" ridge segment, offset from its parent by only 5–6 km. Following the segment naming convention of *Paulatto et al*. [2015] and predecessors [e.g., *Detrick et al*., 1995], the segments currently recognized in the study area include (from north to south) AMAR, AMAR Minor N, AMAR Minor S, and S AMAR (Figure 2). These segments exhibit typical slow spreading ridge morphology with a deep axial valley and relatively well-defined boundary faults with displacements of 100 m or more. Seafloor samples taken from along the ridge axes are basaltic in composition [*Sigurdsson*, 1981; *Stakes et al*., 1984; *Gale et al*., 2013]. Locally, the full spreading rate is ~22 mm/yr [*Argus et al*., 2011] with an opening direction ~16° from the average azimuth of the plate boundary (N104°E) [*DeMets et al*., 2010]. However, because of the staircase nature of the plate boundary, the second-order ridge segments have individual strikes only a few degrees from perpendicular to plate spreading. Separating the two minor segments is the Rainbow nontransform discontinuity, a second-order, 12 km wide offset located at the center of the study area. Just outside the northern and southern boundaries of the study area are two other right-stepping NTDs with offsets of 22 and 43 km, respectively. Mantle Bouguer gravity anomalies (MBA) [*Detrick et al*., 1995; *Thibaud et al*., 1998; *Paulatto et al*., 2015] vary with ridge segmentation, with a large MBA high across the Rainbow NTD and a smaller high at the discontinuity separating S AMAR from AMAR Minor S. The most pronounced MBA lows are located beneath the AMAR, S AMAR, and the southern half of the AMAR Minor S segments. The AMAR Minor N segment corresponds with higher gravity values. Across the two minor segments (in the spreading direction), alternating patterns of high and low gravity and magnetization values correlate with the occurrence of large widely spaced normal faults and tilted crustal blocks.

The Rainbow NTD contains the Rainbow massif, a dome-shaped topographic high rising ~800 m above the axial valley floor. It is considered to be an oceanic core complex; rock samples from its surface mostly consist of ultramafic and gabbroic rocks, with some smaller distributions of basalts [*Fouquet et al*., 1997; *Andreani et al*., 2014]. The massif hosts one of the most active hydrothermal fields along the MAR, the Rainbow hydrothermal field (RHF), with multiple groups of active black smokers and other high-temperature

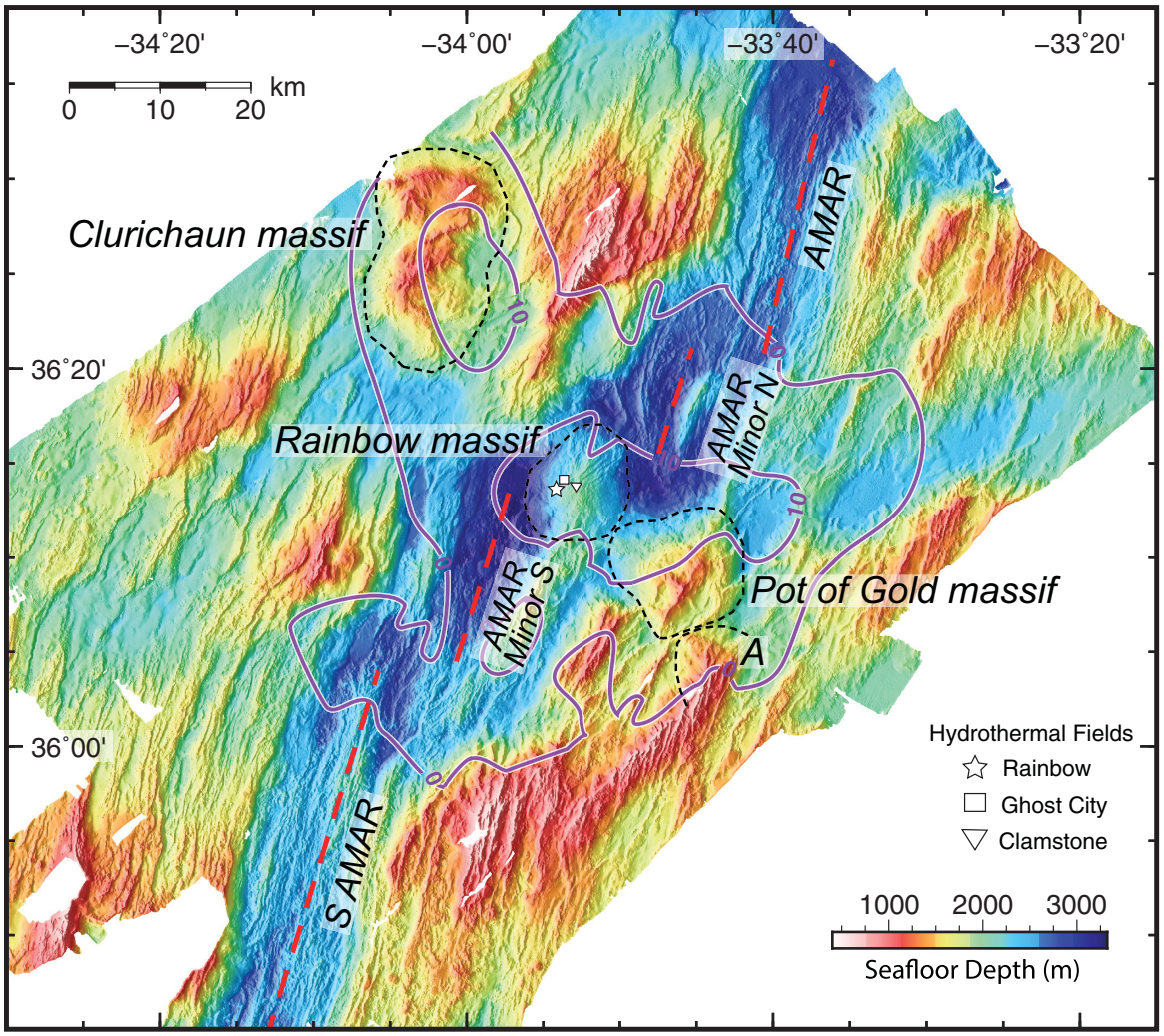

Figure 2. Seafloor bathymetry map of the study area from *Paulatto et al.* [2015]; the bathymetry is shaded by the slope of the seafloor. Dashed red lines denote spreading center segments (labeled). Oceanic core complexes (massifs) are outlined by black dashed lines. Purple lines denote residual mantle Bouguer gravity contour lines of 0 and +10 mGal [*Paulatto et al.*, 2015], indicating anomalously high gravity around the Rainbow NTD and along its off-axis trace.

vents (up to 365°C) [*Fouquet et al.*, 1998; *Charlou et al.*, 2002; *German and Parson*, 1996; *German et al.*, 2010] and an estimated present-day heat flux of 0.5 GW [*German et al.*, 2010]. Despite the predominantly ultramafic composition of the massif, the vent field appears to be driven by a magmatic heat source, as evidenced by its high temperature fluids, flow rates, and chemical composition [*Cann and Strens*, 1982; *Douville et al.*, 2002; *German et al.*, 2010; *Seyfried et al.*, 2011]. In addition to the active field, the massif also hosts two fossil hydrothermal sites: Ghost City, located ~2 km northeast of RHF, and Clamstone, located 2.5 km east of RHF (Figure 2). Both areas are thought to have vented low temperature, metal-poor fluids [*Lartaud et al.*, 2011; *Andreani et al.*, 2014]. Together, the three known sites suggest more than 100 kyr of hydrothermal activity [*Kuznetsov et al.*, 2006; *Lartaud et al.*, 2010, 2011]. Although the Rainbow massif exhibits weakly positive seafloor magnetization in the shipboard data [*Paulatto et al.*, 2015], high-resolution data collected by ROV reveals strong positive magnetic anomalies associated with the ultramafic vent sites [*Szitkar et al.*, 2014].

The Rainbow OCC likely formed by a long-lived west dipping detachment fault whose curved boundary forms the contact between the west flank of the massif and the valley floor [e.g., *Andreani et al.*, 2014]. The location of the detachment breakaway is unknown, but may be located east of the dome given the exposure of mantle rocks and gabbroic intrusions on both the western and eastern flanks of the massif [*Andreani et al.*, 2014]. The massif appears to be linked topographically with the eastern flank of the ridge segment to the south. A set of SW-NE trending faults crosscut the massif, possibly accommodating oblique stresses within the ridge offset [e.g., *Grindlay and Fox*, 1993]. This dense fault network, which appears to be more

recent than the primary detachment faulting, combined with widespread sediment cover on the detachment surface itself, indicate the detachment is no longer active, and the massif has since been split by the newer cross-cutting faults.

In addition to Rainbow, additional possible OCCs have been identified in the study area based on their dome-like topography, local gravity highs, and low magnetization: the Pot of Gold massif located ~15 km southeast of Rainbow, and at least two detachment faults forming an older compound feature whose center is located ~30 km northwest of Rainbow dubbed the Clurichaun massif (Figure 2) [*Paulatto et al*., 2015]. Although their surfaces have not yet been sampled to confirm the presence of lower crustal or mantle rocks, the geophysical data are consistent with a thin-to-nonexistent upper crustal layer. Lying just outside our study area, the NTD at the northern edge of the experiment also contains a massif with outcrops of serpentinized peridotites and gabbroic rocks [*Goud and Karson*, 1985; *Fouquet et al*., 1997; *Gràcia et al*., 2000] and diffuse low-temperature hydrothermal venting [*Dias and Barriga*, 2006].

3. Data and Processing

The multibeam sonar survey covers a total area of ~5400 km^2, centered on the Rainbow massif, extending a total of ~120 km along the plate boundary. The survey includes many closely spaced ship track lines (spaced 1–4 km apart) throughout the central part of the study area, with additional lines carried out at several azimuths, and a sparser outer set of lines that extends to a plate age of almost 2 Myr (Figure 1c). With the closely spaced survey lines, multifold coverage of the seafloor was obtained with a variety of seafloor incidence angles and look directions using the hull-mounted multibeam sonar system of the R/V *Marcus G. Langseth*.

The *Langseth* operated a 12 kHz Kongsberg EM122 system with 432 soundings per swath and two swaths per ping cycle for up to 864 soundings per cycle. To achieve the two swaths per cycle, the transmit fan was duplicated with a small difference in along-track tilt. The system was run with an angular swath width of 124° in an equal area mode, where the beamformer projects beams of varying angle across the swath to create equal size sonar footprints on the seafloor, resulting in a footprint of roughly 20 m and a swath width of 9.4 km in 2500 m of water. The ping rate was 13 s and most survey lines were collected at 4.5 knots, a distance of roughly 30 m per ping cycle, while a fewer number of lines were collected at speeds of up to 8 knots. The system was fully calibrated 8 months prior to the survey and additional patch tests using data from the present survey found no serious problems with the sound-speed profiles used within the system or artifacts due to roll bias or other such effects. As a hull mounted system, the seafloor incidence angles are more vertical than for deep-towed "sidescan" systems, and thus the amplitude of the sonar returns have less dependence on local seafloor slope.

Rather than using the per beam backscatter data, we extracted the higher-resolution seabed image reflectivity data from the raw sonar files. This provides the amplitude information per swath interpolated onto geographically located seafloor positions of a 1024-pixel grid extending across the swath. The EM122 system applies a time varying gain to these data to correct for frequency-dependent attenuation of the signal in the water column, spherical spreading, variations in insonified seafloor area, and a correction for the variation with angle of incidence at the seafloor [*Hammerstad*, 2000]. Data collected during a heavy storm, and when the ship speed dropped below 2 knots (when deploying or recovering ocean bottom seismographs) were removed. Individual swaths were removed where the average amplitude of the swath was anomalously low as compared to an average of neighboring swaths (which can occur due to cavitation and bubble run-down at the transducers). This was accomplished via a MATLAB program using a sliding window technique (along the ship track), with a window length of 21 swaths. On a per swath basis, individual values were removed that exceeded three times the median absolute deviation (MAD) of values for that swath (where the MAD is prescaled by 1.482 to be consistent with one standard deviation for normally distributed data values).

Plots of the raw data showed consistent across track amplitude biases, presumably due to assumptions in the original data handling (the time varying gain corrections) that are not met in reality. The bias generally has the form of too low amplitude near nadir, and too high at larger angles of seafloor incidence, and is roughly symmetric across each swath. However, the shape of the across track bias tends to vary along the ship track, possibly due to changes in water column sound speed, sonar gains, or other factors. Using the

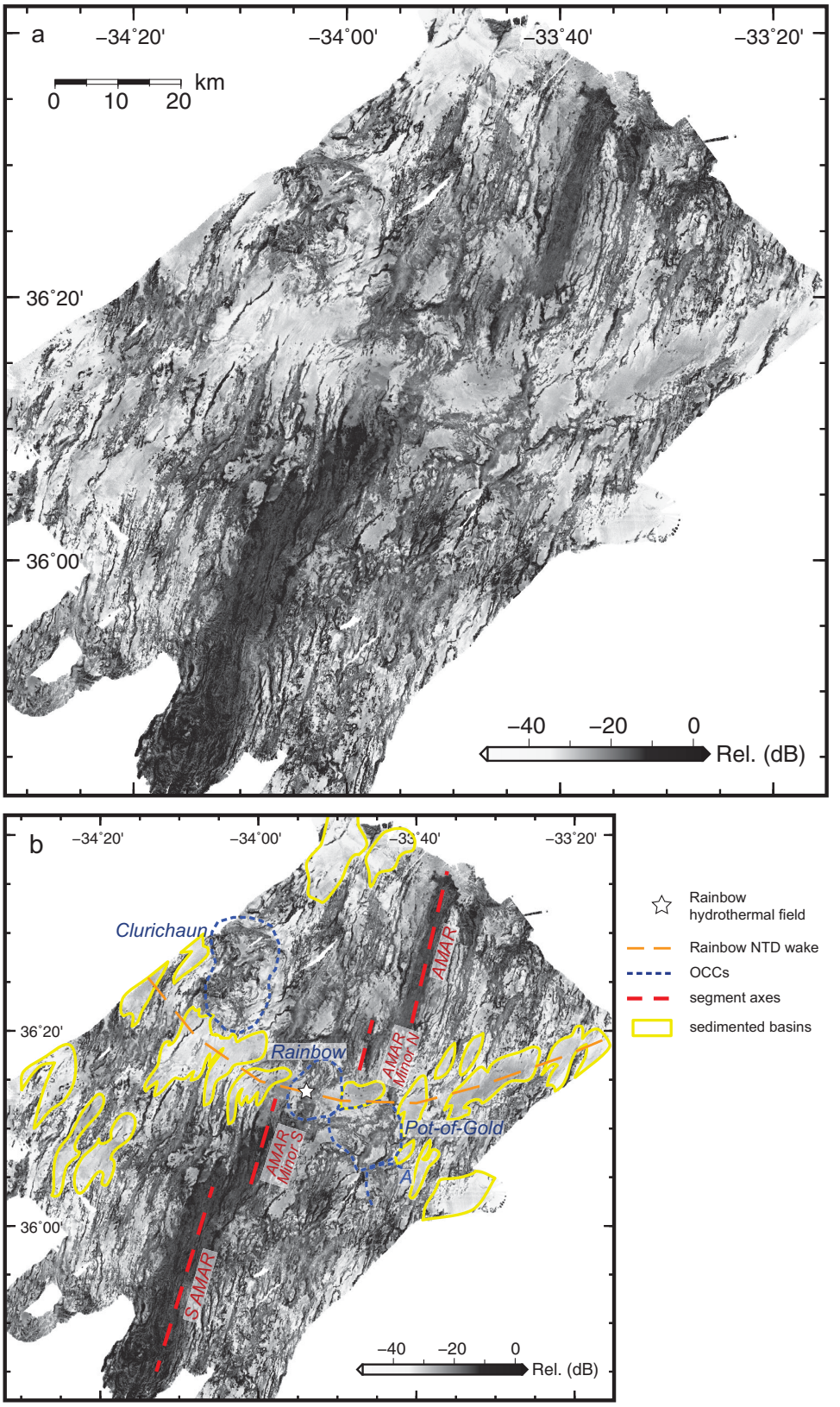

Figure 3. (a) Sonar backscatter image of the study area. Dark colors represent areas of high backscatter intensity and light colors correspond to low backscatter intensity. Effects due to look direction and local seafloor topography have been largely removed, such that the variations in amplitude shown here primarily reflect intrinsic physical properties of the seafloor. (b) Geologic interpretation overlain over sonar backscatter image. Blue dashed lines denote OCCs, and red dashed lines denote spreading center segments. Sedimented basins are outlined in yellow, with the trace of the Rainbow NTD shown by the orange dashed line.

mbbackangle program within the MB-system software package [*Caress and Chayes*, 2014], the average amplitude as a function of seafloor incidence angle was computed for groups of 50 pings along track. This program produces tables of this information for use in the mbprocess program to remove the across-track bias as a function of seafloor incidence angle. However, the tables themselves tend to be affected by data noise and strong changes in seafloor backscatter amplitude, and have jumps in average values between neighboring ping groups that produce jumps in average backscatter amplitude after processing. Therefore, the tables were smoothed both across and along track. First, table outliers exceeding three times the MAD value of that table were removed, and then a smoothing spline was applied as a function of incidence angle (across swath). Then, the tables were smoothed along the ship track via a 17-point triangular-weighted sliding widow. The new correction tables were applied to the data via mbprocess.

The corrected data were gridded with a 60 m spacing using the GMT software [*Wessel et al*., 2013] and its subprograms blockmedian and xyz2grid, to form a single sonar image of the entire survey area. To reduce speckling in the image, a simple despiking algorithm was applied (via a shell programming script) by comparing the processed data values to a smoothed version of the sonar image, removing outliers from the data, and thereafter remaking the sonar image. The effect of this last step on the character of the image was small. Supporting Information that accompanies this paper contains information on the statistics of the data that go into the sonar image, including data density and the spread of data values used to compose each pixel of the sonar image, as well as the estimated standard error of the image. In general, the standard error of the image is ~0.3 dB within the interior of the survey where swaths overlap and ~0.9 dB around the outer perimeter of the survey area where data density is less.

In the survey area, the seafloor depth range is large, varying from 400 to 4000 m, and the sonar image showed a small depth dependence of the amplitudes, with shallower seafloor represented by relatively higher amplitudes and deeper seafloor represented by relatively lower amplitudes. This bias is likely due to an incorrect attenuation model in the time varying gain corrections; the processing assumes a particular water column attenuation model for correcting amplitudes as a function of acoustic energy path length and a deviation in the attenuation model from reality would produce such an artifact. The image amplitudes were adjusted via a simple depth-dependent linear correction. The bathymetry map from *Paulatto et al*. [2015] is shown in Figure 2 and the final seafloor sonar image is shown in Figure 3.

4. Results and Interpretation

After the data processing outlined above, a pass of the ship in one direction produces a similar sonar image as a pass in any other direction for a given area of seafloor. This allowed merging and gridding of the data into a common grid, as is usually done for depth data, with the multifold coverage suppressing noise and remaining data artifacts. This is in contrast to backscatter image mosaics (overlays of data plots from individual ship tracks), which are more commonly presented for sonar amplitude data [e.g., *Escartín et al*., 1999; *Parson et al*., 2000]. Only around the outer perimeter of the sonar image is a faint nadir (near center beam) artifact discernible where overlapping coverage is unavailable. The benefit of this compilation is a complete sonar image whose features can be interpreted as being principally derived from the intrinsic properties of the seafloor rather than from look-direction and seafloor slope.

In the final sonar image (Figure 3), the lighter grays indicate low-amplitude returns and darker grays indicate higher-amplitude returns. Sonar amplitude returns are a measure of how acoustic energy interacts with the seafloor, and depend on a variety of factors, which principally include seafloor density, sound velocity, and bottom roughness (or microtopography) [cf., *Urick*, 1983; *Johnson and Helferty*, 1990; *Lurton et al*., 2015]. The effective acoustic return is a combination of reflected (mirrored from planar surfaces) and diffracted acoustic energy. Direct reflection of the outgoing acoustic pulse usually contributes little to the total energy returned for a moderately sloped seafloor, since this reflection is often directed away from the ship. Instead, the backscattered energy is often dominated by diffraction of sound due to microtopography or material roughness. Materials with a rougher surface backscatter energy more efficiently (producing a higher return) than smoother materials with the same density and acoustic velocity. Seafloor alteration and degree of sedimentation also play important roles, as they lower the density and acoustic velocity of the seafloor, and increase acoustic energy loss. Since the amplitude variations of the sonar image are largely due to the material properties of the seafloor, they are dominated by combinations of seafloor age,

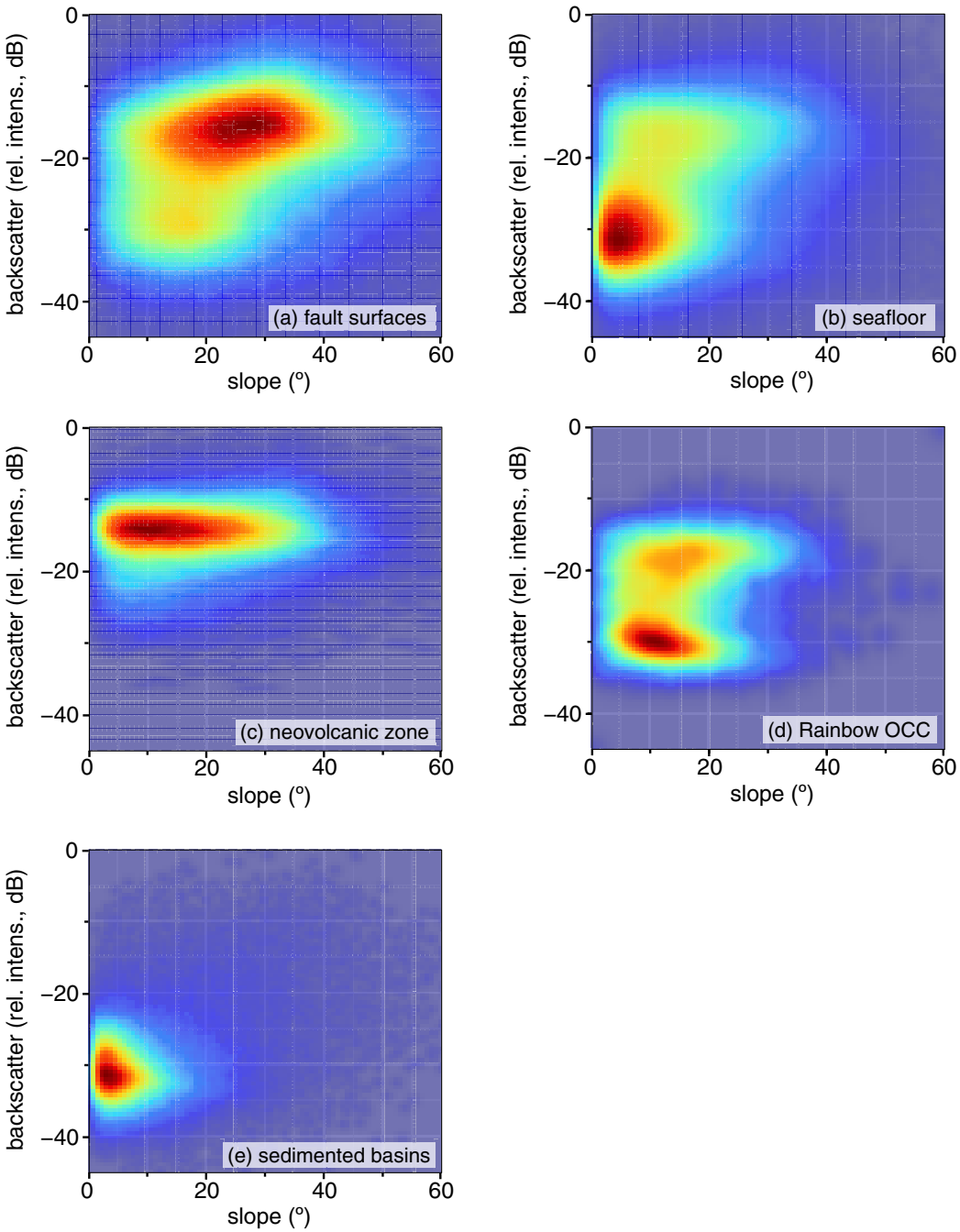

Figure 4. Density distributions of backscatter strength (relative intensity) versus seafloor slope for (a) fault surfaces (as defined by *Paulatto et al.* [2015]), (b) all other seafloor (excluding fault surfaces), (c) the neovolcanic zones, (d) Rainbow OCC, and (e) sedimented basins. The density distributions are shown as heat maps, with red colors corresponding to high density and blue corresponding to low density. Fault surfaces exhibit higher backscatter amplitudes and higher slopes on average than the remaining seafloor. Relatively high backscatter seafloor dominates the neovolcanic zone, which exhibits a much larger range of seafloor slopes and little overlap in relative backscatter intensity compared to the low backscatter, low-angle seafloor that dominates the sedimented basins. Rainbow OCC has a more bimodal distribution in backscatter intensities, with both high and low backscatter amplitudes, but lower amplitudes overall than the neovolcanic zone.

roughness, and sedimentation. Therefore, the lighter colors principally correspond to older, sedimented terrain, especially heavily sedimented basins and areas of sediment located between higher-standing features. The darker colors principally correspond to relatively fresh and/or rough volcanic seafloor (found primarily within the axial valley), along unsedimented fault scarps and fissures, and on the sides and tops of

unsedimented volcanic cones, as well as along many high-standing ridges whose summits we infer to be rugged and/or current-swept.

Submarine features are interpreted on the basis of their amplitude intensity and morphology in the context of other available data. To first order, the image highlights via high amplitudes (darker values) the neovolcanic zones located within the axial valleys of the spreading segments, and faults and steep cones (Figure 3). Large areas of low backscatter define a series of sedimented basins, most of which are arranged in a wide U-shaped pattern in map view, extending away from the Rainbow NTD. The following sections examine some broad characteristics of the sonar image and its correlations with other geophysical data, an exercise that is not generally feasible with typical backscatter image mosaics, and describe and discuss the primary geologic features identified.

4.1. Geophysical Correlations

Paulatto et al. [2015] identified fault surfaces in this area using a bathymetric "slope gradient" method in conjunction with seafloor roughness and an automated edge detection algorithm. Using their fault surface map, we examined the sonar amplitude characteristics of the fault surfaces (which represent approximately 20% of the total survey area) and the remaining seafloor with the fault surfaces removed. Figure 4 shows how bathymetric slope and amplitudes vary for fault surfaces (Figure 4a) and the remaining seafloor (Figure 4b) via frequency distribution plots, or "heatmaps." The identified fault surfaces exhibit higher slopes (typically 20–35°) and higher backscatter amplitudes on average than the remaining seafloor due to lower rates of sediment accumulation on steep slopes and/or more recent surface exposure due to faulting and/or erosional processes. The weak positive correlation between slope and amplitude for fault surfaces suggests that steeper faults are less sedimented on average than shallow ones. A visual comparison of the fault surfaces picked by the algorithm with the sonar data indicates relatively good agreement; however, there are some instances in which hummocky volcanic terrain is incorrectly lumped into a fault surface, or in which the algorithm failed to pick fault surfaces, especially low-angle faults or ones with small throws. The overlapping distributions of the identified fault and nonfault surfaces is expected due to natural variability (e.g., old fault surfaces can be sedimented, not all steep and/or high backscatter surfaces are faults, etc.), but may also partly reflect miscategorization of some seafloor patches by the fault detection algorithm.

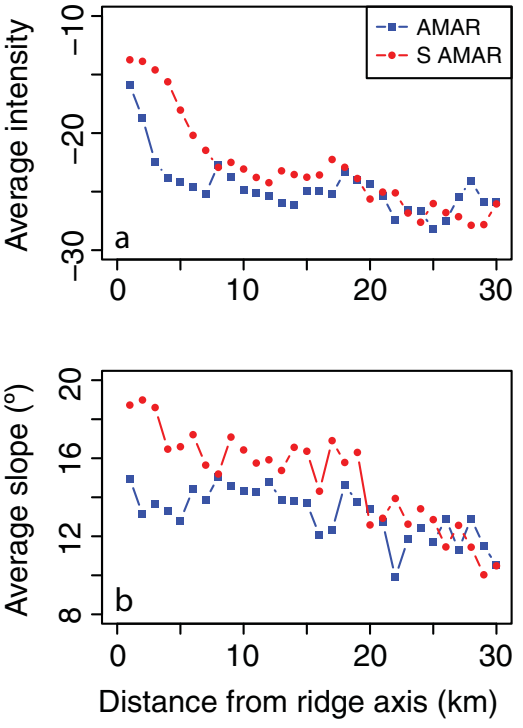

Figure 5. Plots of (a) average (mean) backscatter intensity and (b) average bathymetric slope with distance (age) from the ridge axis (measured parallel to spreading). The standard error of the mean is within the symbol size. Seafloor located off-axis from S AMAR (red) exhibits higher slopes and higher backscatter intensities on average than seafloor formed at the AMAR segment (blue) for the first ~7 km. Beyond 7 km, backscatter intensities of the two main ridge segments are fairly similar and exhibit a modest change with age, while the average slope of the seafloor continues to decrease.

We further subdivide the terrain to examine the sonar data for a few key geological features, including the neovolcanic zone (Figure 4c), the Rainbow OCC (Figure 4d), and the sedimented basins (Figure 4e). The neovolcanic zones are dominated by high-amplitude seafloor with a broad range of seafloor slopes (Figure 4c), while the sedimented basins are characterized by relatively flat terrain with very low backscatter amplitudes, as expected for heavily sedimented seafloor (Figure 4e). The surface of the Rainbow massif exhibits a bimodal distribution in backscatter amplitudes (Figure 4d), with peaks corresponding to the higher backscatter hard rock surfaces, and low backscatter surfaces with significant sediment coverage. The highest amplitude surfaces on Rainbow OCC are lower on average than most of the neovolcanic zone, suggesting more active and recent repaving of the seafloor along the ridge segments than on the oceanic core complex.

Figure 5 shows the average backscatter amplitude and slope as a function of distance from the segment axes (calculated in the spreading direction). The high amplitudes found in the axial valleys are consistent with the formation of relatively fresh seafloor via volcanism, with S AMAR exhibiting higher seafloor amplitudes on average than AMAR. Average amplitudes decline quickly with distance from the ridge axes, and do so at smaller distances for the AMAR ridge segment as compared to S AMAR (Figure 5a), in accordance with a narrower neovolcanic zone along the AMAR segment. After 7–8 km of spreading and sediment accumulation, average amplitudes are nearly the same for these two ridge segments, though S AMAR continues to show slightly higher backscatter likely due to its more rugged terrain (Figure 5b). Moving further off-axis, the change in average intensity flattens significantly—it appears that once the seafloor reaches a certain age and has accumulated a significant amount of sediment, further sedimentation and alteration has a declining effect on backscatter intensities.

4.2. Volcanic Terrain

The sonar image is dominated by the high-amplitude neovolcanic zones that define the active ridge segments. These accretionary zones primarily consist of extrusive volcanic terrain, with an irregular, hummocky morphology, a mottled appearance in the sonar image, and a few larger and smoother lava flows, flat-topped cones, and seamounts. This terrain is further characterized by fine-scale lineations that can be constructional (formed by fissure eruptions) and/or tectonic (formed by small-scale faulting) in nature; differentiating between the two is not always possible at the resolution of the data. The bathymetric map shows a number of AVRs within the axial valleys of both AMAR (Figure 6) and S AMAR (Figure 7), some of which were previously identified by *Stakes et al*. [1984] and *Parson et al*. [2000]. Despite being areas of increased crustal construction (as inferred by their shallow topography), the AVRs are largely indistinguishable from the rest of the neovolcanic zone in the sonar backscatter image. Their hummocky, mottled appearance resembles much of the surrounding seafloor, with fine, ridge-parallel faulting evident even here at the center of the neovolcanic zone.

The ridge segments in the study area exhibit differences in seafloor properties that suggest differences in volcanic accretion processes and/or long-term magma supply. The AMAR neovolcanic zone is narrower (∼2.5–4 km) than at S AMAR and AMAR Minor S (∼4–6 km) (Figures 3 and 5a), indicating that recent volcanism along this ridge segment has occurred over a more confined area than south of Rainbow. Relatively few high backscatter volcanics extend outside the innermost axial valley walls along the AMAR segment. This is in contrast with S AMAR, where high backscatter volcanics are common beyond the first major set of normal faults and the neovolcanic zone occupies a larger proportion of the axial valley. The AMAR segment also exhibits lower backscatter on average than the southern S AMAR and AMAR Minor S segments (Figures 3 and 5a). These results, combined with the deeper bathymetry and lower seafloor magnetization (Figures S5 and S6 in Supporting Information) along AMAR, strongly suggest lower overall magma supply along this segment than south of Rainbow (see section 5.1).

AMAR Minor N is the most poorly defined segment in the backscatter image (Figures 3 and 6) and appears to be less volcanically active than the other segments in the study area. The small NTD between AMAR and AMAR Minor N segment has little off-axis trace, indicating this ridge offset formed very recently. There is only one small patch of higher backscatter material associated with this segment that does not appear to be a fault surface (marked A, Figure 6c), and it is not as high amplitude as some extrusives found on the other ridge segments. Central to this ridge segment and extending along the majority of its length is a large westward dipping normal fault with significant throw and rotated topography. The fault (B, Figure 6c) has a peak throw of nearly 1 km and its surface exhibits high backscatter, suggesting recent exposure by active faulting and/or mass wasting. Its surface has a convex shape similar to that of major OCC-forming detachment faults.

Individual ridge segments show an asymmetry between the bounding faults and the neovolcanic zone, with AMAR exhibiting the most pronounced effect (Figure 6). The center of magmatic activity near the segment ends does not correspond with the center of the axial valley, but is instead slightly offset toward the inside corners of the ridge-NTD-ridge system, resulting in an oblique alignment of the axial neovolcanic zone with respect to the azimuth of the segment axes as defined by the bounding faults. This trend is a few degrees closer to the oblique regional trend of the plate boundary as compared with the bounding faults, which on average are nearly perpendicular to spreading. A similar asymmetry has been described in the seabed magnetization anomaly map of the area [*Paulatto et al*., 2015], which shows a ridge axis anomaly

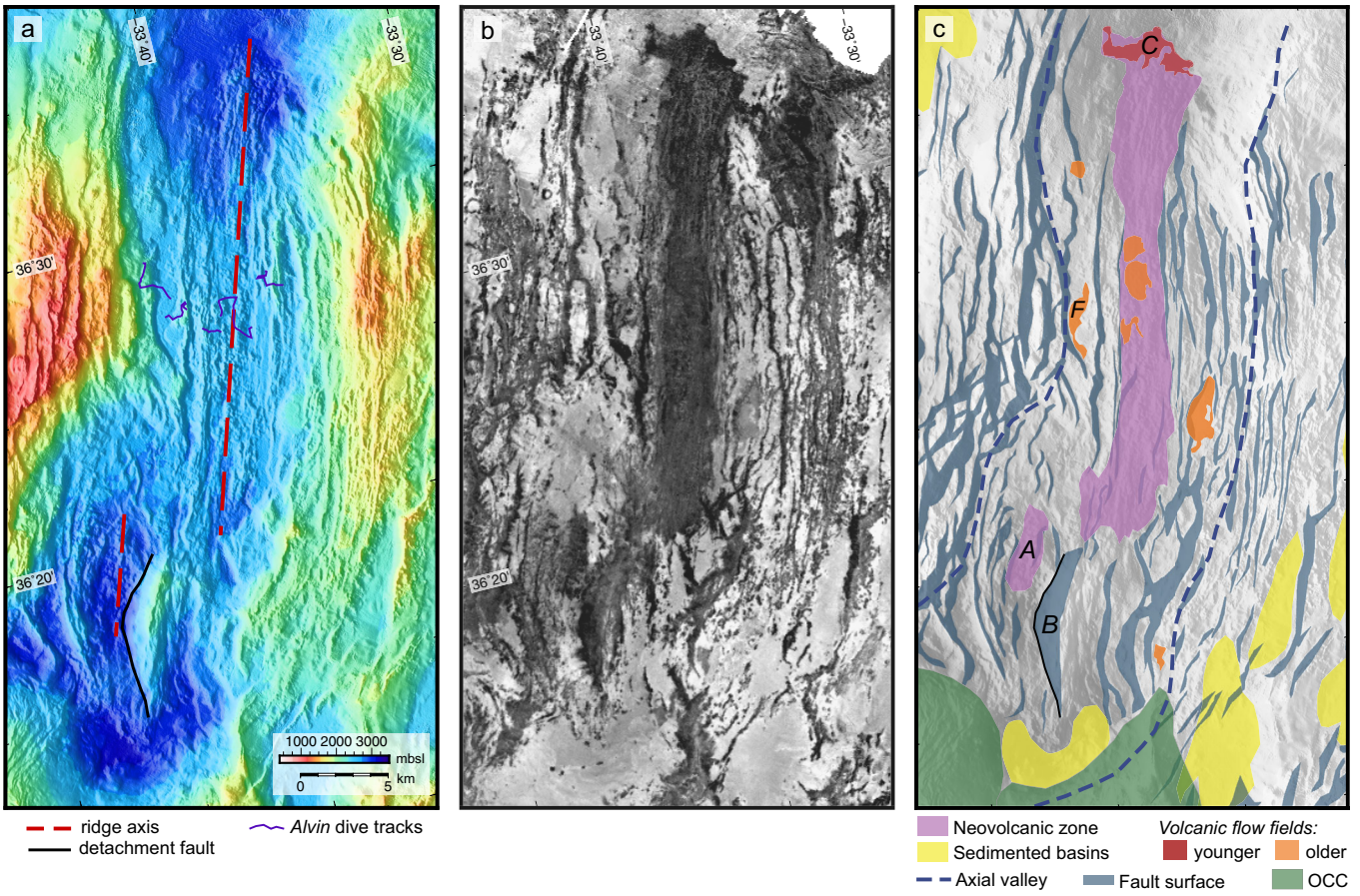

Figure 6. Maps of (a) bathymetry, (b) backscatter intensity, and (c) corresponding geologic interpretation of the AMAR and AMAR Minor N segments (located north of the Rainbow offset). Dark purple lines in (a) mark approximate locations of ALVIN dives (based on map in *Stakes et al.* [1984]). Thick black line denotes western edge of proposed nascent detachment fault. (c) Dark blue dashed line denotes the main bounding walls of the axial valley. Colored fields denote sedimented basins (yellow), the Rainbow and Pot of Gold OCCs (green), neovolcanic zones (light purple), and identified volcanic flow fields (orange and red). The red flow fields exhibit higher backscatter and are likely some of the youngest identifiable units. Fault surfaces [*Paulatto et al.*, 2015] shown in light blue. Labels mark some specific features discussed in the text, including AMAR Minor N's small neovolcanic zone (A) and large offset normal fault (B), the particularly high backscatter volcanic unit we identify at the northern end of AMAR (C), and an off-axis volcanic unit with ALVIN observations (F).

roughly centered on the high-backscatter neovolcanic zone. This obliquity between the neovolcanic zones and the more sinuous bounding faults of the axial valley has been noted previously [*Spencer et al.*, 1997; *Parson et al.*, 2000] and may be common in this region of the MAR and/or along oblique spreading centers in general. It may indicate that the bounding faults are strongly controlled by the opening direction and thus align nearly perpendicular to spreading, while the azimuth of the neovolcanic zones more strongly reflects the general trend of the underlying magmatic system.

Outside the axial valley, the seafloor alternates between the relatively steep, smooth terrain that characterizes fault surfaces, and the rougher volcanic terrain topping large tilted fault blocks. Variations in fault spacing previously identified in *Paulatto et al.* [2015] are visible in the sonar image: the AMAR segment tends to be more finely faulted than the segments further south, particularly on its eastern flank, where faults are closely spaced with relatively small offsets (Figure 6), while S AMAR and AMAR Minor S have wider-spaced faults on average with significantly larger throws (up to ~1.4 km) (Figure 7). Fault spacing increases and fault surfaces become less steep on average toward the ridge offsets. Local areas of high backscatter immediately adjacent to faults are interpreted as slump or debris deposits unless they possess clear topographic features that distinguish them as constructional. Volcanic cones show up in the image as high contrast circular features, sometimes cut by faulting.

4.2.1. Lava Flow Fields and Seafloor Morphology

One challenge of interpreting backscatter data is that because it is dependent on a number of parameters such as sediment thickness, seafloor morphology, fine-scale seafloor texture, and rock alteration, it is not

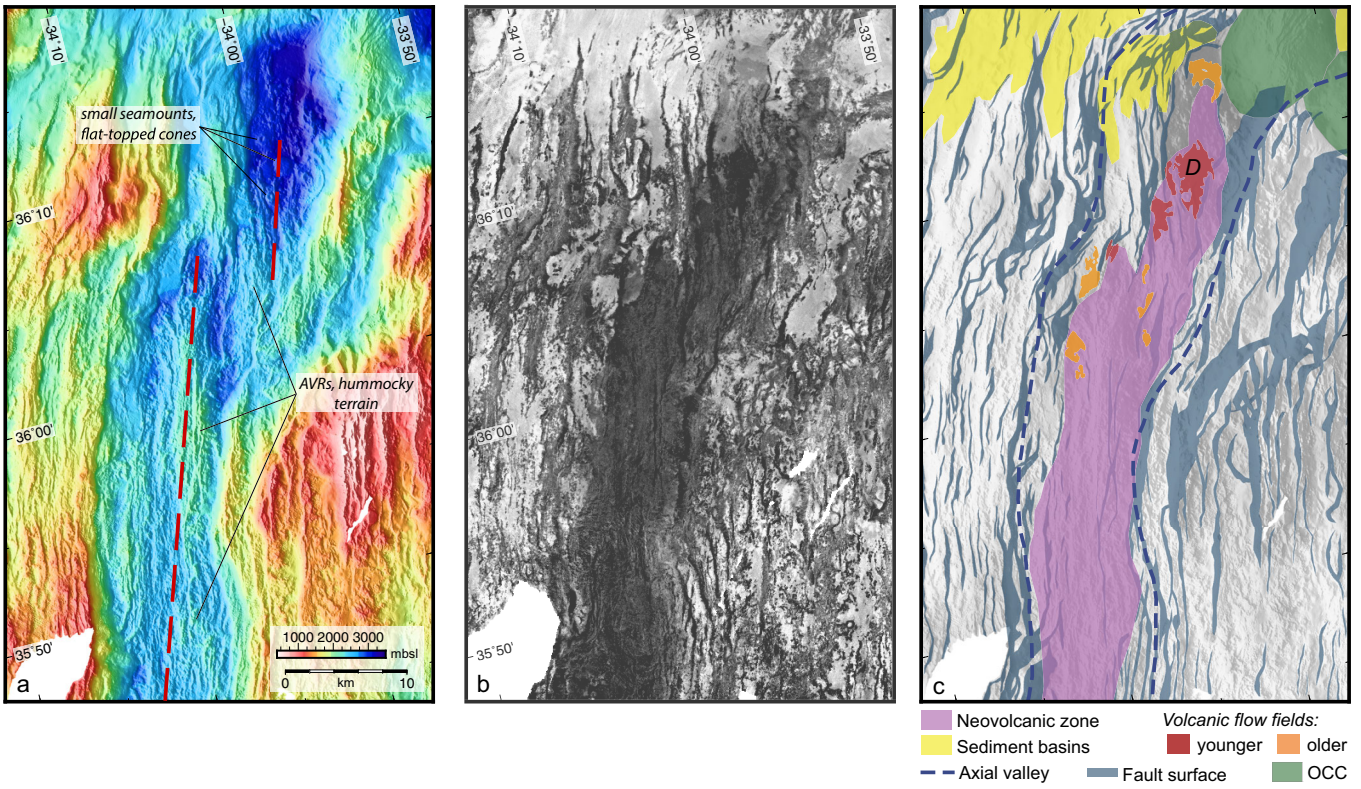

Figure 7. Maps of (a) bathymetry, (b) backscatter intensity, and (c) corresponding geologic interpretation of the S AMAR and AMAR Minor S segments (located south of the Rainbow offset). Fields and symbols as in Figure 6. Label D denotes high backscatter unit discussed in text.

generally possible to directly invert backscatter amplitudes for parameters of interest like eruptive age, flow morphology, etc. However, variations in backscatter amplitude within the neovolcanic zone and nearby terrain enable us to distinguish differences in relative age and/or texture of the seafloor in some locations. We therefore identify some of the volcanic flow fields visible in the sonar image, relying on amplitude and topographic relations as well as similarities in seafloor texture to define the extent of single contiguous units. We also used slope masks and worked primarily on seafloor with low angle topography (~15° or less) to help ensure identification of constructional surfaces rather than fault surfaces and other steep slopes and/or associated debris flows, all of which can exhibit high backscatter. This exercise requires some degree of conjecture in places, and determining whether these "units" consist of single or multiple eruptions and refining their boundaries would require more detailed observations and higher resolution mapping, sampling and imaging than is currently available—we therefore refer to these features as "flow fields" to distinguish them from true eruptive units. We also draw on additional seafloor observations in the study area from human-occupied submersible dives [*Stakes et al*., 1984] (approximate dive tracks shown in Figure 6a) and deep-tow sidescan sonar (TOBI) data [*Parson et al*., 2000] as we discuss the results of the sonar imaging below.

Of the flow fields we identify in the sonar image, the ones with the highest backscatter (thus presumably some of the youngest) occur near the ends of ridge segments, where the long-term magma supply inferred from seafloor depth, gravity, and estimated crustal thickness is lower. These flow fields are located at the ends of the AMAR (C, Figure 6c) and AMAR Minor S (D, Figure 7c) segments, adjacent to the heavily sedimented basins that mark the ridge offsets. The flow field at the northernmost end of the AMAR segment (C, Figure 6c) was identified in the TOBI mapping of *Parson et al*. [2000] as being fresh sheet flows and hummocks, while some of the high backscatter units in AMAR Minor S (D, Figure 7c) were identified as being fresh flat flows. While we are unaware of any direct bottom observations of these flow fields, we interpret them as having minimal sediment cover and likely younger than the surrounding terrain. Both areas are associated with strong seafloor magnetization (Figures S5 and S6 in Supporting Information) [*Paulatto et al*., 2015], and are characterized by relatively flat seafloor topography (or in the case of the unit in AMAR Minor S, a broad flat region topped by a small seamount). The relatively flat portions of these flow fields contrast

with the more hummocky character of most of the volcanic terrain, suggesting they might be dominated by more fluid sheet or lobate flows.

Aside from the unusually high backscatter flow field identified at the northern end of the segment, the rest of AMAR's neovolcanic zone exhibits only moderately high sonar amplitudes and weakly positive seafloor magnetization (Figure S5 in Supporting Information), consistent with relatively low eruption recurrence rates. Like many segments of the Mid-Atlantic Ridge, the terrain is dominated by a hummocky texture, composed by many overlapping volcanic mounds and/or cones [e.g., *Briais et al*., 2000; *Smith et al*., 1995]. This is consistent with the observations of *Parson et al*. [2000], who map the central part of AMAR's axial valley as faulted or sedimented hummocks, and all locations in central AMAR with direct visual dive observations were described as heavily faulted with moderate sediment coverage [*Stakes et al*., 1984]. Meanwhile, some low-lying areas in between hummocky ridges and cones tend to be flatter and show higher backscatter. Bottom observations of the central portion of the AMAR segment using *DSV Alvin* indicate these lows are filled by relatively flat sheet or lobate flows, while the hummocky terrain is built of steep mounds of pillow lava [*Stakes et al*., 1984]. In some exposures the sheet flows and pillows were described as being interlayered and/or transitioning between flow morphologies, indicating they sometimes form from the same eruption.

Some identified flow fields are located outside the main neovolcanic zone (Figures 5 and 6). Although none of these flows look "fresh" as compared to seafloor within the neovolcanic zone, they do exhibit moderately high backscatter relative to their immediate surroundings. Observations on one of these flow fields (F in Figure 6c) found a large sheet and lobate flow sufficiently sedimented that the relatively flat-lying flow was rarely visible except where buckled plates protrude through [*Stakes et al*., 1984]. This area is also associated with slightly stronger seafloor magnetization (Figure S5 in Supporting Information). This suggests they may have erupted slightly outside the main volcanic zone, or at least later than the surrounding seafloor. While higher backscatter than some of its immediate surroundings, its backscatter intensity is similar to or lower than most of the adjacent neovolcanic zone (Figure 6).

There are also some notable differences in eruption style between the different ridge segments. While all ridge segments are dominated by hummocky volcanic terrain, with myriad mounds and small cones visible in the bathymetry, most of the largest volume cones and seamounts are located along the AMAR Minor S and AMAR segments. The seamounts visible along S AMAR are mostly found off-axis near the trace of the Rainbow NTD (i.e., erupted near the end of the ridge segment). Seamounts appear to be more abundant and larger volume near segment ends than at their centers. This focused style of volcanism has been found to correspond with relatively long-lived, low effusion rate eruptions, sometimes from deep crustal magma chambers, and is characteristic of regions with low and/or episodic magma supply [e.g., *Colman et al*., 2012].

The discrepancy between the locations of the most recent identified volcanics (near the segment ends) and the regions with the highest long-term crustal accumulation (segment centers) may be in part due to the difference in sampling timescales—the sonar amplitude data provide a snapshot of processes on a much shorter timescale than the long term variations in crustal accumulation that lead to significantly thicker crusts and shallower axial topography at segment centers than segment ends. Additionally, we only identify flow fields that are large enough to form visually coherent patches of seafloor in the sonar images, so recent volcanic units that are too small to confidently distinguish from the rugged surrounding terrain will be missed. The southern end of S AMAR has a broad area of particularly high backscatter (Figure 3) as well as the strongest positive magnetic anomaly in the study area (Figure S6 in Supporting Information), suggesting relatively recent seafloor renewal, but individual flow fields are not well defined here. While this may be in part due to worse data coverage (ship turns and associated higher data noise in this location), it is also likely that volcanic units are harder to identify in the sonar image due to small eruptive volumes and more variable, rugged terrain (see section 5.1).

Many of the highest-amplitude volcanics correspond to areas in the neovolcanic zone with smoother than average seafloor topography, suggesting that lava flow morphology (not just sediment coverage) may contribute to the amplitude variations observed in the neovolcanic zone. We are therefore cautious about ascribing relative ages to these features, but we hypothesize that the apparent correlation between backscatter and seafloor morphology is at least in part due to the fact that more recent eruptions are not yet as modified by faulting and fissuring as the surrounding seafloor and so may have a smoother character in both the bathymetry map and the sonar image. While one might be tempted to draw the conclusion that

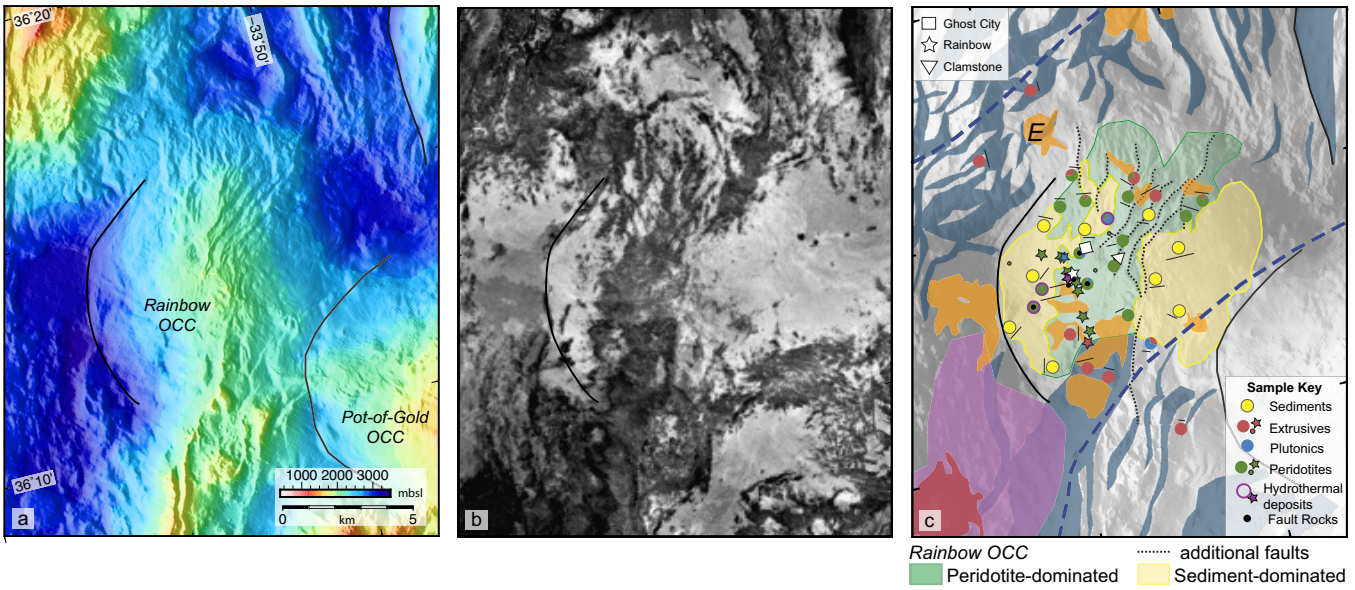

Figure 8. (a) Bathymetry and (b) backscatter intensity images of the Rainbow massif area, with (c) corresponding geologic interpretation. Thick solid lines denotes western edge of the detachment faults for Rainbow, Pot of Gold, and the proposed nascent detachment in AMAR Minor N. Active (Rainbow) and fossil hydrothermal fields shown as white symbols. Sample data from dredges (short straight black lines denote dredge locations, large circles show corresponding approximate percentage sample type for that dredge) and submersible dives (stars) from compilation of *Andreani et al.* [2014]. Colored fields denote domains of sediment-dominated (yellow) and peridotite-dominated (green) surfaces of the massif. Higher backscatter patches interpreted to be extrusive basalts are shown in orange. Label E denotes an area of high backscatter seafloor interpreted to be a volcanic unit draping the saddle that connects Rainbow massif to the ridge topography to the northwest (discussed in text). All other fields and symbols as in Figures 6 and 7.

older eruptions tend to be dominated by hummocky pillow lavas and more recent ones tend to be smoother sheets and lobates, we note that (1) older sheets and lobates are more likely to have been buried or overprinted by more recent eruptions than older cones and pillow mounds, and (2) any recently constructed hummocky terrain might be harder to identify in the sonar image both because it is inherently more variable and because such eruptions tend to pile up in a smaller area for a given volume eruption (in addition to possibly being smaller volume on average to begin with—see section 5.1 for further discussion). We therefore suspect a sampling bias and do not recognize a temporal variation in lava morphology.

4.3. Sedimented Basins

A series of broad, topographically flat, low-backscatter areas define the off-axis trace of the Rainbow NTD (Figure 3). Their flat morphology and low backscatter amplitudes indicate they are heavily sedimented basins. Though occasionally cut by topographic highs extending from adjacent abyssal hill topography, the U-shaped string of basins is visible in the amplitude, bathymetry, and gravity data, all of which indicate a long history of low magma supply at this ridge offset. On the basis of the azimuth of this pattern, the NTD migrated southward at a rate of ~6 mm/yr up until about 1 Ma [*Paulatto et al.*, 2015], when it appears to have slowed or even stopped. In addition to the Rainbow NTD wake, another smaller series of sedimented basins is visible south of the main Rainbow NTD wake, located roughly ~26–40+ km off-axis (Figure 3). Although near the edge of the study area, the trace of this second wake appears to continue off-axis in satellite-derived bathymetric data (Figure 1b). Its relationship to the Rainbow NTD wake indicates that there may have been a second, smaller ridge offset just south of the Rainbow NTD that then merged with the Rainbow offset, eliminating a small intervening ridge segment. The two sets of sedimented basins appear to merge just east of the Pot of Gold massif (Figure 3), at roughly 1.1 Ma, and approximately coincident with the slowing of the southward migration of the Rainbow NTD.

4.4. Core Complexes

The OCCs identified in the study area have a mottled appearance in the backscatter image, with highly variable amplitudes (Figure 3). Rainbow massif and the two newly identified candidate OCCs (Pot of Gold and Clurichaun) all have significant but patchy sediment cover. Their summits and steeper flanks tend to have higher backscatter indicative of a rocky seafloor, and all OCCs show signs of syn- and/or postexhumation faulting and mass wasting. In addition, a small area immediately southeast of Pot of Gold (labeled A in

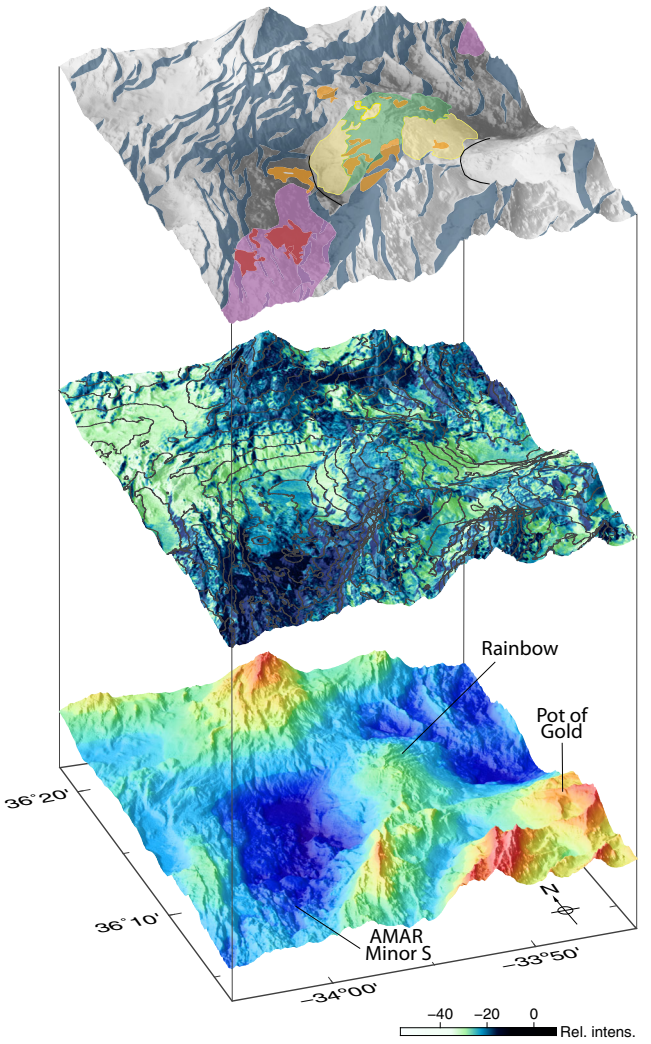

Figure 9. Three-dimensional perspective views of bathymetry (bottom), backscatter intensity draped over bathymetry (middle), and geologic interpretation (top) for the Rainbow area (view across AMAR Minor S and the Rainbow OCC from the SW; vertical exaggeration: 2×). Backscatter image (middle): light greens correspond to low backscatter intensity, dark blues correspond to high backscatter intensity, and gray lines denote 200 m contours of water depth. The sonar images are shaded by the slope of the bathymetry. Colored fields as in Figure 8. See Figure S8 in Supporting Information for additional view from the NE.

Figure 2) has a similar appearance to the other identified OCCs in both the backscatter image and bathymetry data, including a dome-like topography, large faults that link up with the ridge to the southwest, and a mottled appearance with a patchy terrain that disrupts the regional lineations (Figures 2 and 3). Although much smaller than the other OCCs, and currently unsampled, it is possible this feature represents yet another point on the continuum between detachment initiation and a fully developed core complex.

The Rainbow massif shows variations in backscatter amplitude (Figures 8 and 9) that correlate well with faulting patterns and seafloor sample compositions. Some of the higher backscatter areas, particularly in the NE quadrant and summit region of the massif, highlight the SW-NE trending fault surfaces that crosscut the massif [*Lartaud et al.*, 2010; *Andreani et al.*, 2014], and likely reflect both steeper slopes and more freshly exposed surfaces. Apart from this faulting, the rest of the massif can be broadly divided into three backscatter categories with low, moderately high, and high amplitudes, which correspond well with areas dominated by sediments, peridotites, and basalts, respectively. The western and eastern flanks of the Rainbow massif have low backscatter surfaces, and seafloor samples (and dive observations) in these areas are dominated by sediments (yellow circles in Figure 8c). A moderately high backscatter region runs north to south across the massif summit; samples from this area are dominated by exposed serpentinized peridotites and gabbros (green and blue circles in Figure 8c). A few subregions on the massif, particularly on the SW flank, exhibit even stronger backscatter amplitudes, and correlate with regions where basalts have been sampled either by dredging or ROV work [*Fouquet et al.*, 1998; *Fouquet and IRIS Scientific Party*, 2001; *Andreani et al.*, 2014]. While it is possible some of these basalts are klippen of volcanic seafloor rafted up by the detachment fault, we note that many of these patches are located west (and down-slope) of various peridotite exposures, and the presumed trace of the detachment break-away. If these features are pieces of volcanic seafloor that predate the detachment, they require a very complex break-away geometry and/or significant postuplift deformation. At least a few of these patches exhibit cone-like features in the bathymetry suggestive of constructional features. We therefore interpret these subregions as extrusive units that likely postdate exhumation of the surrounding peridotites and plutonics. The high saddle that connects Rainbow massif to the ridge topography to the northwest (labeled E in Figure 8c) also has patches of the seafloor that look constructional and likely postdate faulting, with either a lava flow or debris flow extending down the presumed

trace of the detachment fault into the sedimentary basin west of Rainbow massif. These patches have a similar backscatter to the basaltic units identified on the massif, though quite mottled in appearance; the saddle is not sufficiently well-sampled to confirm the proportions of rock types here, but dredges in this vicinity have recovered both mantle rocks and basalts (Figure 8c).

5. Discussion

5.1. Magma Supply and Crustal Accretion

Many of the variations in volcanism and faulting observed along this section of the MAR can be discussed in terms of the interplay between magmatic and tectonic activity. The broad axial valleys and relatively wide volcanic zones are typical of other ridge segments along the MAR, whose neovolcanic zones are as much as ~12 km wide [e.g., *Parson et al*., 2000]. Segments north of the study area and close to the Azores hot spot exhibit shallower axial topography with narrower axial floors and smaller axial valley walls [e.g., *Blondel*, 1996; *Parson et al*., 2000], and have been described as having fresher lavas with higher backscatter on average than segments in this study area [*Parson et al*., 2000]. These observations are consistent with higher magma supply along the ridge due to the presence of the Azores hot spot. However, while ridge segments near the Azores exhibit higher inferred magma supply than the current study area, there does not appear to be a systematic northward trend of increasing supply either within the study area or immediately north of it [*Parson et al*., 2000]. The southernmost segment in our study area, S AMAR, has the highest inferred magma supply based on every geophysical proxy available, suggesting that any long-wavelength influence in magma supply from the Azores hot spot is weak relative to local controls on magma supply.

5.1.1. Magma Supply by Segment

The four ridge segments in the study area exhibit differences in time-averaged magma supply. The shallower axial valley, lower gravity, stronger seafloor magnetization, and higher average backscatter neovolcanic zone of S AMAR indicate this segment has had a higher average magma supply than the other ridge segments in the study area, at least in the recent past. At nearly 40 km long, S AMAR is also longer than the other segments (~10–25 km), consistent with previous findings that ridge segmentation length scales often correlate with differences in inferred magma supply [e.g., *Langmuir et al*., 1986; *Sinton et al*., 1991]. AMAR, the second longest segment, has the second largest magma supply based on its moderately shallow bathymetry, while the shorter AMAR Minor S is much deeper on average (i.e., low long-term magma supply) but contains the largest area of recent (high backscatter) identifiable flow fields. Although AMAR Minor S appears to have been recently active, we emphasize that eruption recurrence rates are relatively low here, and an instantaneous observation need not reflect the long-term average. The smallest and youngest segment, AMAR Minor N, is relatively amagmatic, showing only a small patch of moderately recent volcanic extrusives (labeled A in Figure 6c). Perhaps somewhat counter-intuitively, we identify more flow fields in the sonar image in areas with lower magma supply than in the higher magma supply S AMAR segment. This may in part reflect the tendency of eruptions to be larger and occur less frequently at low magma supply [e.g., *White et al*., 2002, 2009; *Colman et al*., 2012], making them more likely to be distinguishable from their surroundings, while the higher magma supply S AMAR may be expected to have more frequent but smaller eruptions, making them harder to identify in the sonar image due to their small size and less significant age differences. Seafloor morphology may also play a role in generating these differences, with S AMAR largely characterized by hummocky volcanic fields that result in a more rugged, variable terrain than the smoother terrain near the segment ends. This observation was also made by *Parson et al*. [2000], and recent studies of AVRs suggest their hummocky terrain is primarily constructed by small volume eruptions that produce single cones or volcanic lineaments (short series of cones inferred to lie above eruptive fissures) [*Searle et al*., 2010], making them difficult to identify individually in the sonar image.

5.1.2. Intrasegment Variations

The prevailing model is that ridge segment centers typically have higher magma supplies on average than segment ends [e.g., *Detrick et al*., 1995]. This is consistent with the shallower bathymetry and lower gravity near the segment centers in this study area, but would not be evident from the backscatter data alone. The highest-amplitude (and by inference some of the youngest) flow fields identified in the sonar image are located along AMAR Minor S and at the northern end of the AMAR segment, areas that have relatively low time-averaged magma supply based on bathymetry and gravity data. AMAR and S AMAR both exhibit hourglass-shaped axial valleys that widen and deepen toward the segment ends, suggestive of a robust

magma supply at the segment centers. This hourglass shape is somewhat echoed by the high backscatter region of the neovolcanic zones, but overall these high backscatter zones define more linear trends on the seafloor than the axial valleys and their bounding faults. AMAR in particular displays a relatively straight neovolcanic zone with only a slight broadening at the segment ends.

5.1.3. Volcanic Processes and Eruptive Style

Lava flow morphology, eruptive style, frequency, and volume have been shown to correlate with magma supply along mid-ocean ridges. Regions with low magma supply tend to have less frequent but larger volume eruptions than regions with higher magma supply [e.g., *White et al*., 2009; *Colman et al*., 2012], and are more likely to produce long-lived eruptions from focused (point source) vents, with lava morphologies thought to be associated with low effusion rates [e.g., *Bonatti and Harrison*, 1988; *Gregg and Fink*, 1995]. The observations in the study area are consistent with this relationship: many of the largest volume seamounts are found near the ends of ridge segments (either on-axis or near the off-axis trace of the ridge offset) where magma supply is expected to be lower. While the sample coverage in the study area is not sufficient for a detailed analysis of this segment-scale variability, petrologic studies elsewhere have suggested that segment ends are also associated with the deepening of magma chambers [e.g., *Eason and Sinton*, 2006; *Herzberg*, 2004]. Samples from the very high backscatter unit at the northern tip of AMAR Minor S exhibit low CaO/Al_2O_3 ratios for the area (data from *Gale et al*. [2013]), suggesting an earlier onset of clinopyroxene fractionation that could be due to higher pressure crystallization. Some samples from the AMAR segment also exhibit the high-Al, low-Si chemical signature that has been attributed to high pressure ($\sim$0.3–0.4 GPa) crystallization and strongly associated with other areas of low magma supply (e.g., ridge terminations and slow spreading ridges) [*Eason and Sinton*, 2006; *Herzberg*, 2004].

5.2. OCC Formation and Evolution

Melt supply is thought to be one of the primary factors controlling the formation and evolution of oceanic detachment faults. Earlier numerical models estimate that long-lived, low-angle detachment faults tend to form when $\sim$30–50% of the extension at a spreading ridge is accommodated by magmatic accretion [*Buck et al*., 2005; *Behn and Ito*, 2008; *Tucholke et al*., 2008], although more recent simulations suggest that a key factor in the formation of detachment faults is how magmatic accretion is partitioned between intrusions into the brittle crust and magma emplacement below the brittle-ductile transition, rather than the total amount of magma supply [*Olive et al*., 2010]. This suggests that the prevalence of these features in ridge offsets such as the Rainbow NTD reflects the combination of low rates of diking and magmatic extrusion, and high tectonic strain found there.

In the current study area, large detachment faults have repeatedly formed along the inside corners bordering the Rainbow NTD where magma supply is relatively low, leading to OCC (and OCC-like features) formation along the wake of the NTD. The appearance of OCCs in the southeast inside corner of the ridge-NTD-ridge offset spatially coincides with the change in the Rainbow NTD's migration and possible merging of a smaller NTD. Since then, multiple detachment faults have formed on the southern inside corner, each connected to the southern ridge flank by faults with large heave and separation, and each just northwest of the previous one. Each detachment fault accrued up to a few kilometers of displacement before shutting off. No OCCs have been identified on the outside corners of the ridge offsets.

The conditions that lead to detachment faulting on the southeast inside corner may be migrating northward. North of the now presumably inactive Rainbow detachment fault, the AMAR Minor N segment exhibits low volcanic activity with only one small patch of high-backscatter seafloor indicative of recent volcanism in the central north, higher gravity than the neighboring ridge segments consistent with relatively thin crust, and a large, apparently active fault spanning most of the length of the segment near its center. This fault is the dominant feature in the axial valley, with a curved convex shape similar to major OCC-forming detachment faults, and almost 1 km of throw accumulated to date. We therefore identify this fault surface as a possible nascent detachment fault occurring along a relatively magma-starved section of the ridge. With continued low levels of volcanic activity, the fault system may eventually evolve into a full-fledged detachment and exhume another OCC. Similar features have been found elsewhere [e.g., *Escartín et al*., 1999; *Searle et al*., 1998].

Extrusive basalts have been recognized on Rainbow OCC previously [*Fouquet et al*., 1998; *Andreani et al*., 2014], but their extent and continuity are poorly known. The new backscatter image indicates they may pave a significant portion of the SW flank of the massif (Figures 8 and 9), with additional small outcroppings

in other areas as well. Their sonar amplitudes are similar to areas in the neovolcanic zone that were identified by *Stakes et al*. [1984] and/or *Parson et al*. [2000] as having moderate sediment cover, and are most likely not recently erupted. Basalts recovered from the massif show various extents of alteration [*Fouquet et al*., 1998; *Andreani et al*., 2014] and seem to postdate the formation of the massif. Their presence may be yet another indication that extension is no longer accommodated by detachment faulting, but instead by some combination of the newer cross-cutting faults and some minor amounts of magmatic intrusion into the base of the Rainbow massif and nearby. Volcanic fields have been found on the large-offset detachment surfaces of other OCCs [e.g., *Tucholke et al*., 2001; *Dick et al*., 2008], likely indicating melt intrusion into the footwall during or after exhumation.

6. Conclusions

We present a new compilation of seafloor sonar reflectivity centered on the Rainbow NTD of the Mid-Atlantic Ridge. Dense sonar coverage allowed for merging and gridding of the data into a common grid, as is usually done for depth data, with the multifold coverage suppressing noise and data artifacts typical of standard backscatter image mosaics. The resulting sonar image can be interpreted as being principally derived from the intrinsic properties of the seafloor rather than from look-direction and seafloor slope.

We examine the sonar image in the context of other geophysical datasets to examine seafloor properties and identify volcanic and tectonic features. The S AMAR segment has a wider neovolcanic zone with higher average backscatter intensities than AMAR, consistent with the higher magma supply inferred based on the shallow bathymetry and strong seafloor magnetization. AMAR Minor N has the lowest inferred magma supply, with only a small patch of high backscatter seafloor and active faulting within the axial valley.

Differences in volcanic activity, faulting, eruption style, and frequency also correlate with inferred magma supply on the scale of individual ridge segments. Segment centers are dominated by hummocky volcanic terrain constructed by many individual volcanic cones and lineaments, sometimes forming AVRs. The ends of ridge segments are thought to have lower time-averaged magma supply and tend to be associated with larger volume flow fields and seamounts, smoother volcanic terrain, and more widely spaced faults than segment centers. Individual volcanic flow fields are also easier to distinguish in low supply areas, likely due to larger volume eruptions on average and longer recurrence intervals, leading to greater amplitude contrasts to the surrounding seafloor.

A series of large detachment faults have formed a series of oceanic core complexes along the wake of Rainbow NTD, with a possible new detachment fault now developing in the small ridge segment just north of the now inactive Rainbow OCC. On Rainbow massif, areas of high, moderately high, and low backscatter intensity seafloor are spatially correlated with observations of basalt, gabbro/peridotite, and sediment, respectively.

Acknowledgments

We thank the shipboard scientific party and crew of R/V *Marcus G. Langseth* Leg MGL1305 for their help with the data acquisition. The sonar data were processed using a combination of the software packages MB-system (version 5.3.2017) [*Caress and Chayes*, 2014], GMT (version 4.5.6) [*Wessel et al*., 2013], and MATLAB (version 8.4.0.) (Natick, Massachusetts: The MathWorks Inc., 2014). The data used for these analyses are available from the Marine Geoscience Data System database (http://www.marine-geo.org/index.php). This research was supported by National Science Foundation grants OCE-0961151 (R.A.D.) and OCE-0961680 (J.P.C. and R.A.S.). This is SOEST contribution #9693.

References

Andreani, M., J. Escartín, A. Delacour, B. Ildefonse, M. Godard, J. Dyment, A. E. Fallick, and Y. Fouquet (2014), Tectonic structure, lithology, and hydrothermal signature of the Rainbow massif (Mid-Atlantic Ridge 36°N14′N), *Geochem. Geophyst. Geosyst*, *15*, 3543–3571, doi: 10.1002/2014GC005269.

Argus, D. F., R. G. Gordon, and C. DeMets (2011), Geologically current motion of 56 plates relative to the no-net-rotation reference frame, *Geochem. Geophys. Geosyst.*, *12*, Q11001, doi:10.1029/2011GC003751.

Behn, M.D., and G. Ito (2008), Magmatic and tectonic extension at mid-ocean ridges: 1. Controls on fault characteristics, *Geochem. Geophys. Geosyst.*, *9*, Q08O10, doi:10.1029/2008GC001965.

Behn, M. D., J. Lin, and M. T. Zuber (2002), Mechanisms of normal fault development at mid-ocean ridges, *J. Geophys. Res.*, *107*(B4), 2083, doi:10.1029/2001JB000503.

Blondel, P. (1996), Segmentation of the Mid-Atlantic Ridge south of the Azores, based on acoustic classification of TOBI data, in *Tectonic, Magmatic, Hydrothermal and Biological Segmentation of Mid-Ocean Ridge*, edited by C. J. MacLeod et al., *Geol. Soc. Spec. Publ.*, *118*, 17–28.

Bonatti, E., and C.G.A. Harrison (1988), Eruption styles of basalts in oceanic spreading ridges and seamounts: Effect of magma temperature and viscosity, *J. Geophys. Res.*, *93*(B4), 2967–2980.

Briais, A., H. Sloan, L. Parson, and B. Murton (2000), Accretionary processes in the axial valley of the Mid-Atlantic Ridge 27°N–30°N from TOBI side-scan sonar images, *Mar. Geophys. Res.*, *21*, 87–119.

Buck, W. R., L. L. Lavier, and A. N. B. Poliakov (2005), Modes of faulting at mid-ocean ridges, *Nature*, *434*, 719–723.

Canales, J. P., R. S. Detrick, J. Lin, J. A. Collins, and D. R. Toomey (2000), Crustal and upper mantle seismic structure beneath the rift mountains and across a nontransform offset at the Mid-Atlantic Ridge (35°N), *J. Geophys. Res.*, *105*(B12), 2699–2719, doi:10.1029/1999JB900379.

Canales, J. P., et al. (2013), MARINER: Seismic investigation of the rainbow hydrothermal field and its tectono/magmatic setting, Mid-Atlantic Ridge 36°14′N—A report from RV M.G. Langseth Cruise MGL1305, *InterRidge News*, *22*, 46–52.

Cann, J. R., and M. R. Strens (1982), Black smokers fuelled by freezing magma, *Nature*, *298*, 147–149, doi:10.1038/298147a0.
Cann, J. R., D. K. Blackman, D. K. Smith, E. McAllister, B. Janssen, S. Mello, E. Avgerinos, A. R. Pascoe, and J. Escartín (1997), Corrugated slip surfaces formed at ridge-transform intersections on the Mid-Atlantic Ridge, *Nature*, *385*, 329–332.
Cannat, M., et al. (1995), Thin crust, ultramafic exposures, and rugged faulting patterns at the Mid-Atlantic Ridge (22°–24°N), *Geology*, *23*, 49–52.
Cannat, M., et al. (1999), Mid-Atlantic Ridge-Azores hotspot interactions: Along-axis migration of a hotspot-derived event of enhanced magmatism 10 to 40 Ma ago, *Earth Planet. Sci. Lett.*, *173*, 257–269.
Caress, D. W., and D. N. Chayes (2014), MB-System: Mapping the seafloor, Monterey Bay Aquarium Research Institute, Moss Landing, CA, and Lamont-Doherty Earth Observatory, Columbia University, N. Y. [Available at www.mbari.org/data/mbsystem and www.ldeo.columbia.edu/res/pi/MB-System.]
Charlou, J. L., J. P. Donval, Y. Fouquet, P. Jean-Baptiste, and N. Holm (2002), Geochemistry of high H2 and CH4 vent fluids issuing from ultramafic rocks at the Rainbow hydrothermal field (36°14′N, MAR), *Chem. Geol.*, *191*(4), 345–359.
Cheadle, M., and C. Grimes (2010) To fault or not to fault, *Nat. Geosci.*, *3*, 454–456.
Colman, A., et al. (2012), Effects of variable magma supply on mid-ocean ridge eruptions: Constraints from mapped lava flow fields along the Galápagos Spreading Center, *Geochem. Geophys. Geosyst.*, *13*, Q08014, doi:10.1029/2012GC004163.
DeMets, C., R. G. Gordon, and D. F. Argus (2010), Geologically current plate motions, *Geophys. J. Int.*, *181*, 1–80.
Detrick, R. S., H. D. Needham, and V. Renard (1995), Gravity anomalies and crustal thickness variations along the Mid-Atlantic Ridge between 33°N and 40°N, *J. Geophys. Res.*, *100*(B3), 3767–3787, doi:10.1029/95JB0249.
Dias, A. S., and F. J. A. S. Barriga (2006), Mineralogy and geochemistry of hydrothermal sediments from the serpentinite-hosted Saldanha hydrothermal field (36°34′N, 33°26′W) at MAR, *Mar. Geol.*, *225*(1–4), 157–175.
Dick, H. J. B., M. A. Tivey, and B. E. Tucholke (2008), Plutonic foundation of a slow-spreading ridge segment: Oceanic core complex at Kane Megamullion, 23°30′N, 45°20′W, *Geochem. Geophys. Geosyst.*, *9*, Q05014, doi:10.1029/2007GC001645.
Douville, E., J. J. Charlou, E. H. Oelkers, P. Bienvenu, C. F. J. Colon, J. P. Donval, Y. Fouquet, D. Prieur, and P. Appriou (2002), The Rainbow vent fluids (36°14′N, MAR): The influence of ultramafic rocks and phase separation on trace metal content in Mid-Atlantic Ridge hydrothermal fluids, *Chem. Geol.*, *184*, 37–48.
Eason, D. E., and J. M. Sinton (2006), Origin of high-Al N-MORB by fractional crystallization in the upper mantle beneath the Galápagos Spreading Center, *Earth Planet. Sci. Lett.*, *252*, 423–436.
Escartín, J., and J. P. Canales (2011), Detachments in oceanic lithosphere: Deformation, magmatism, fluid flow and ecosystems, *Eos Trans. AGU*, *92*(4), 31.
Escartín, J., P. A. Cowie, R. C. Searle, S. Allerton, N. C. Mitchell, C. J. MacLeod, and P. A. Slootweg (1999), Quantifying tectonic strain and magmatic accretion at a slow-spreading ridge segment, Mid-Atlantic Ridge, 29°N, *J. Geophys. Res.*, *104*, 10,421–10,437.
Escartín, J., D. K. Smith, J. Cann, H. Schouten, C. H. Langmuir, and S. Escrig (2008), Central role of detachment faults in accretion of slow-spreading oceanic lithosphere, *Nature*, *455*, 790–794, doi:10.1038/nature07333.
Fouquet, Y., and IRIS Scientific Party (2001) IRIS cruise report, IFREMER, Plouzane, France.
Fouquet, Y., et al. (1997), Discovery and first submersible investigations of the rainbow hydrothermal field on the MAR (36°14′N), *EOS Trans. AGU*, *78*, 832.
Fouquet, Y., et al. (1998), FLORES diving cruise with the Nautile near the Azores—First dives on the Rainbow field: Hydrothermal seawater/mantle interaction, *InterRidge News*, *7*(1), 24–28.
Gale, A., C. A. Dalton, C. H. Langmuir, Y. Su, and J.-G. Schilling (2013), The mean composition of ocean ridge basalts, *Geochem. Geophys. Geosyst.*, *14*, 489–518, doi:10.1029/2012GC004334.
German, C. R., and L. M. Parson (1996), Hydrothermal exploration near the Azores Triple Junction: Tectonic control of venting at slow-spreading ridges? *Earth Planet. Sci. Lett.*, *138*, 93–104.
German, C. R., A. M. Thurnherr, J. Knoery, J. L. Charlou, P. Jean-Baptiste, and H. N. Edmonds (2010), Heat, volume and chemical fluxes from submarine venting: A synthesis of results from the Rainbow hydrothermal field, 36 N MAR, *Deep Sea Res., Part I*, *57*(4), 518–527.
Goud, M. G., and J. A. Karson (1985), Tectonics of short-offset, slow-slipping transform zones in the FAMOUS area, Mid-Atlantic Ridge, *Mar. Geophys. Res.*, *7*, 489–514.
Gràcia, E., J. C. Charlou, J. Radford-Knoery, and L. M. Parson (2000), Non-transform offsets along the Mid-Atlantic Ridge south of the Azores (38°N-34°N): Ultramafic exposures and hosting of hydrothermal vents, *Earth Planet. Sci. Lett.*, *177*, 89–103.
Gregg, T. K. P., and J. H. Fink (1995), Quantification of submarine lava-flow morphology through analog experiments, *Geology*, *23*(1), 73–76.
Grindlay, N. R., and P. J. Fox (1993), Lithospheric stresses associated with nontransform offsets of the Mid-Atlantic Ridge: Implications from a finite element analysis, *Tectonics*, *12*(4), 982–1003.
Grindlay, N. R., P. J. Fox, and K. C. Macdonald (1991), Second-order ridge axis discontinuities in the south Atlantic: Morphology, structure, and evolution, *Mar. Geophys. Res.*, *13*(1), 21–49.
Grove, T. L., R. J. Kinzler, and W. B. Bryan (1992), Fractionation of mid-ocean ridge basalt (MORB), in *Mantle Flow and Melt Generation at Mid-Ocean Ridges*, edited by J. Phipps Morgan, D. K. Blackman, and J. M. Sinton, *AGU Monogr.*, vol. 71, pp. 281–310, AGU, Washington, D. C.
Hammerstad, E. (2000), Backscattering and seabed image reflectivity, *EM Tech. Note*, 5 pp., Kongsberg Maritime AS, Horten, Norway.
Herzberg, C. (2004), Partial crystallization of mid-ocean ridge basalts in the crust and mantle, *J. Petrol.*, *45*, 2389–2405.
Hooft, E. E., R. S. Detrick, D. R. Toomey, J. A. Collins, and J. Lin (2000), Crustal thickness and structure along three contrasting spreading segments of the Mid-Atlantic Ridge, 33.5°–35°N, *J. Geophys. Res.*, *105*, 8205–8226, doi:10.1029/1999JB900442.
Ildefonse, B., D. K. Blackman, B. E. John, Y. Ohara, D. J. Miller, C. J. MacLeod, and Shipboard Scientific Party (2007), Oceanic core complexes and crustal accretion at slow-spreading ridges, *Geology*, *35*, 623–626.
Johnson, H. P., and M. Helferty (1990), The geological interpretation of side-scan sonar, *Rev. Geophys.*, *28*(4), 357–380.
Kuznetsov, K., G. Cherkashev, A. Lein, V. Shilov, F. Maksimov, K. Arslanov, and D. Tarasenko (2006), ^{230}Th/U dating of massive sulfides from the Logatchev and Rainbow hydrothermal fields (Mid-Atlantic Ridge), *Geochronometria*, *25*(5), 51–55.
Langmuir, C. H., J. F. Bender, and R. Batiza (1986), Petrological and tectonic segmentation of the East Pacific Rise, 5 30′–14 30′N, *Nature*, *322*, 422–429.
Lartaud, F., et al. (2010), Fossil clams from a serpentinite-hosted sedimented vent field near the active smoker complex Rainbow, MAR, 36°13′N: Insight into the biogeography of vent fauna, *Geochem. Geophys. Geosyst.*, *11*, Q0AE01, doi:10.1029/2010GC003079.
Lartaud, F., C. T. S. Little, M. De Rafelis, G. Bayon, J. Dyment, B. Ildefonse, Y. Fouquet, F. Gaill, and N. Le Bris (2011), Fossil evidence for serpentinization fluids fueling chemosynthetic assemblages, *Proc. Natl. Acad. Sci. U.S.A.*, *108*, 7968–7703, doi:10.1073/pnas.1009383108.
Lurton, X., G. Lamarche (Eds.) (2015), Backscatter measurements by seafloor-mapping sonars: Guidelines and recommendations, GeoHab Backscatter Working Group report, 200 pp. [Available at http://geohab.org/wp-content/uploads/2014/05/BSWG-REPORT-MAY2015.pdf.]

Macdonald, K. C., D. S. Scheirer, and S. M. Carbotte (1991), Mid-ocean ridges: Discontinuities, segments and giant cracks, *Science*, *253*, 986–994.
Olive, J. A., M. D. Behn, and B. E. Tucholke (2010), The structure of oceanic core complexes controlled by the depth distribution of magma emplacement, *Nat. Geosci.*, *3*(7), 491–495.
Parson, L., E. Gracia, D. Coller, C. German, and D. Needham (2000), Second-order segmentation; the relationship between volcanism and tectonism at the MAR, 38°N-35°40′N, *Earth Planet. Sci. Lett.*, *178*, 231–251.
Paulatto, M., J. P. Canales, R. A. Dunn, and R. A. Sohn (2015), Heterogeneous and asymmetric crustal accretion: New constraints from multi-beam bathymetry and potential field data from the Rainbow area of the Mid-Atlantic Ridge (36°15′N), *Geochem. Geophys. Geosyst.*, doi: 10.1002/2015GC005743, in press.
Phipps Morgan, J., and D. W. Forsyth (1988), Three-dimensional flow and temperature perturbations due to a transform offset: Effects on oceanic crustal and upper mantle structure, *J. Geophys. Res.*, *93*(B4), 2955–2966.
Sauter, D., M. Cannat, S. Rouméjon, M. Andreani, D. Birot, A. Bronner, and R. Searle (2013), Continuous exhumation of mantle-derived rocks at the Southwest Indian Ridge for 11 million years, *Nat. Geosci.*, *6*(4), 314–320, doi:10.1038/ngeo1771.
Schilling, J.-G., M. Zajac, R. Evans, T. Johnston, W. White, J.D. Devine, and R. Kingsley (1983), Petrology and chemical variations along the Mid-Atlantic Ridge from 29°N to 73°N, *Am. J. Sci.*, *283*, 210–586.
Searle, R. C., P. A. Cowie, N. C. Mitchell, S. Allerton, C. J. MacLeod, J. Escartín, S. M. Russell, P. A. Slootweg, and T. Tanaka (1998), *Earth Planet. Sci. Lett.*, *154*, 167–183.
Searle, R. C., et al. (2010), Structure and development of an axial volcanic ridge: Mid-Atlantic Ridge, 45°N, *Earth Planet. Sci. Lett.*, *299*, 228–241.
Seher, T., W. C. Crawford, S. C. Singh, M. Cannat, V. Combier, and D. Dusunur (2010), Crustal velocity structure of the Lucky Strike segment of the Mid-Atlantic Ridge at 378N from seismic refraction measurements, *J. Geophys. Res.*, *115*, B03103, doi:10.1029/2009JB006650.
Sempéré, J.-C., J. Lin, H. S. Brown, H. Schouten, and G. M. Purdy (1993), Segmentation and morphotectonic variations along a slow-spreading center: The Mid-Atlantic Ridge (24″00′N-30″40′N), *Mar. Geophys. Res.*, *15*, 153–200.
Seyfried, W. E., N. J. Pester, K. Ding, and M. Rough (2011), Vent fluid chemistry of the Rainbow hydrothermal system (36°N, MAR): Phase equilibria and in situ pH controls on subseafloor alteration processes, *Geochim. Cosmochim. Acta*, *75*, 1574–1593.
Shaw, P. R. (1992), Ridge segmentation, faulting and crustal thickness in the Atlantic Ocean, *Nature*, *358*, 490–493, doi:10.1038/358490a0.
Shaw, P. R., and J. Lin (1993), Causes and consequences of variations in faulting style at the Mid-Atlantic Ridge, *J. Geophys. Res.*, *98*, 21,839–21,851, doi:10.1029/93JB01565.
Sigurdsson, H. (1981), First-order major element variation in basalt glasses from the Mid-Atlantic Ridge—29°N to 73°N, *J. Geophys. Res.*, *86*(B10), 9483–9502.
Sinton, J. M., S. M. Smaglik, J. J. Mahoney, and K. C. Macdonald (1991), Magmatic, processes at superfast spreading mid-ocean ridges: Glass compositional variations along the East Pacific Rise, 13–23°S, *J. Geophys. Res.*, *96*(B4), 6133–6155.
Smith, D. K., et al. (1995), Mid-Atlantic Ridge volcanism from deep-towed side-scan sonar images, 25°-29°N, *J. Volcanol. Geotherm. Res.*, *67*, 233–262.
Spencer, S., D. K. Smith, J. R. Cann, J. Lin, and E. McAllister (1997), Structure and stability of non-transform discontinuities on the Mid Atlantic Ridge between 24°N and 30°N, *Mar. Geophys. Res.*, *19*, 339–362.
Stakes, D. S., J. W. Shervais, and C. A. Hopson (1984), The volcanic-tectonic cycle of the FAMOUS and AMAR Valleys, Mid-Atlantic Ridge (36°47′N): Evidence from basalt glass and phenocryst compositional variations for a steady state magma chamber beneath the valley midsections, AMAR 3, *J. Geophys. Res.*, *89*, 6995–7028.
Szitkar, F., Y. Fouquet, C. Honsho, and H. Horen (2014), The magnetic signature of ultramafic-hosted hydrothermal sites, *Geology*, *43*, 87–90, doi:10.1130/G35729.1.
Thibaud, R., P. Gente, and M. Maia (1998), A systematic analysis of the Mid-Atlantic Ridge morphology between 15°N and 40°N: Constraints of the thermal structure, *J. Geophys. Res.*, *103*(B10), 24,233–24,243.
Tolstoy, M., A. J. Harding, and J. A. Orcutt (1993), Crustal thickness on the Mid-Atlantic Ridge: Bull's-eye gravity anomalies and focused accretion, *Science*, *262*, 726–729, doi:10.1126/science.262.5134.726.
Tucholke, B. E., J. Lin, and M. C. Kleinrock (1998), Megamullions and mullion structure defining oceanic metamorphic core complexes on the Mid-Atlantic Ridge, *J. Geophys. Res.*, *103*, 9857–9866.
Tucholke, B. E., K. Fujioka, T. Ishitara, G. Hirth, and M. Kinoshita (2001), Submersible study of an oceanic megamullion in the central North Atlantic, *J. Geophys. Res.*, *106*(B8), 16,145–16,161, doi:10.1029/2001JB000373.
Tucholke, B. E., M. D. Behn, W. R. Buck, and J. Lin (2008), Role of melt supply in oceanic detachment faulting and formation of megamullions, *Geology*, *36*(6), 455–458.
Urick, R. J. (1983), *Principles of Underwater Sound for Engineers*, 3rd ed., McGraw-Hill, N. Y.
Wessel, P., W. H. F. Smith, R. Scharroo, J. F. Luis, and F. Wobbe (2013), Generic mapping tools: Improved version released, *EOS Trans. AGU*, *94*, 409–410.
White, S. M., K. C. Macdonald, and J. M. Sinton (2002), Volcanic mound fields on the East Pacific Rise, 16°–19°S: Low effusion rate eruptions at overlapping spreading centers for the past 1 Myr, *J. Geophys. Res.*, *107*(B10), 2240, doi:10.1029/2001JB000483.
White, S. M., J. L. Mason, K. C. Macdonald, M. R. Perfit, V. D. Wanless, and E. M. Klein (2009), Significance of widespread low effusion rate eruptions over the past two million years for delivery of magma to the overlapping spreading centers at 9°N East Pacific Rise, *Earth Planet. Sci. Lett.*, *280*, 175–184.
Yeo, I., R. C. Searle, K. L. Achenbach, T. P. Le Bas, and B. J. Murton (2012), Eruptive hummocks: Building blocks of the upper ocean crust, *Geology*, *40*, 91–94.